Measurement and Interpretation of Eddy Currents Induced in a Segmented Conducting Wall by MHD Instabilities in a Tokamak

Andrea M. V. Garofalo

Thesis advisor:

Professor Michael E. Mauel

Submitted in partial fulfillment of the requirements

for the degree of Doctor of Philosophy

in the Graduate School of Arts and Sciences

COLUMBIA UNIVERSITY

1997

Contents

To my parents, Enza and Salvatore, and
to my love, Suzanne

Acknowledgments

I would like to thank both Michael Mauel, my thesis advisor, and Gerald Navratil, the project director, for their support and inspiring guidance throughout this research.

Thanks also to J. Manickam and Morrell Chance for lending their codes and for providing generous assistance, and to Tom Ivers, Steve Sabbagh and M.K. Vijaya Sankar for the innumerable times they shared their knowledge with me.

My gratitude to the technical staff of HBT-EP and all of my colleagues who have contributed to this work: Maurice Cea, Nicholas Rivera, Estuardo Rodas, Hank Alvestad, Raed Kombargi, Qingjun Xiao, Ned Eisner, Dave Nadle, Dave Maurer, Erik Taylor, Alberto Sainz.

Finally, I would like to thank my family and relatives who have provided me with constant support and encouragement during the past six years.

Measurement and Interpretation of Eddy Currents Induced in a Segmented Conducting Wall by MHD Instabilities in a Tokamak

Andrea M. V. Garofalo

Submitted in partial fulfillment of the requirements

for the degree of Doctor of Philosophy

in the Graduate School of Arts and Sciences

COLUMBIA UNIVERSITY

1997

Abstract

Measurement and Interpretation of Eddy Currents Induced in a Segmented Conducting Wall by MHD Instabilities in a Tokamak

Andrea M. V. Garofalo

The characteristics of external kink instabilities observed during wall stabilization studies in HBT-EP have been compared with the predictions of ideal MHD theory in order to gain more understanding of the stabilizing role of a resistive wall that is segmented both toroidally and poloidally. The reconstructed equilibria, for different plasma-wall configurations, are consistent with the numerous external and internal magnetic measurements, and the measured soft x-ray profiles and equilibrium eddy currents. The stability analysis of these equilibria predicts, for a model wall that is continuous and perfectly conducting, patterns of instability-induced eddy currents that are in excellent agreement with the ones observed on the actual HBT-EP wall. These eddy current patterns account for the stabilization of fast ideal modes that is observed when the wall is fully inserted, consistently with the prediction of the marginal stability boundary.

1

Introduction

1.1. Fusion and Tokamaks

"My son, be warned! Neither soar too high, lest the sun melt the wax; nor swoop too low, lest the feathers be wetted by the sea" (Ovid: *Metamorphoses),* said Daedalus with tears in his eyes to his son Icarus. Soon afterwards, as they were flying toward Sicily, Icarus disobeyed his father, and began soaring toward the sun, rejoiced by the lift of his great sweeping wings. But the heat of the sun melted the wax that held in place the feathers, and Icarus fell in the sea and drowned.

In a common interpretation of this myth, Icarus symbolizes, in his defiance of the sun, human intellect in open rebellion against the limitations imposed on men by the gods. The same intense attitude towards the sun is certainly a large component of what, in the past fifty years, has inspired men in the effort to reproduce on earth the thermonuclear fusion reactions that power the sun, to exploit them as commercial source of electricity.

Developing a completely new source of energy such as fusion is, indeed, a formidable scientific and technological task, which requires the solutions to a number of challenging physics as well as engineering problems.

At the high temperatures necessary to bring like-charged nuclei to fuse (about 100 million degrees centigrade), the gas of the fuel elements is highly ionized (a state that is called *plasma*), and cannot be efficiently confined by material walls. In a tokamak (see Fig. 1.1), the plasma is confined in a toroidal chamber by a magnetic field.

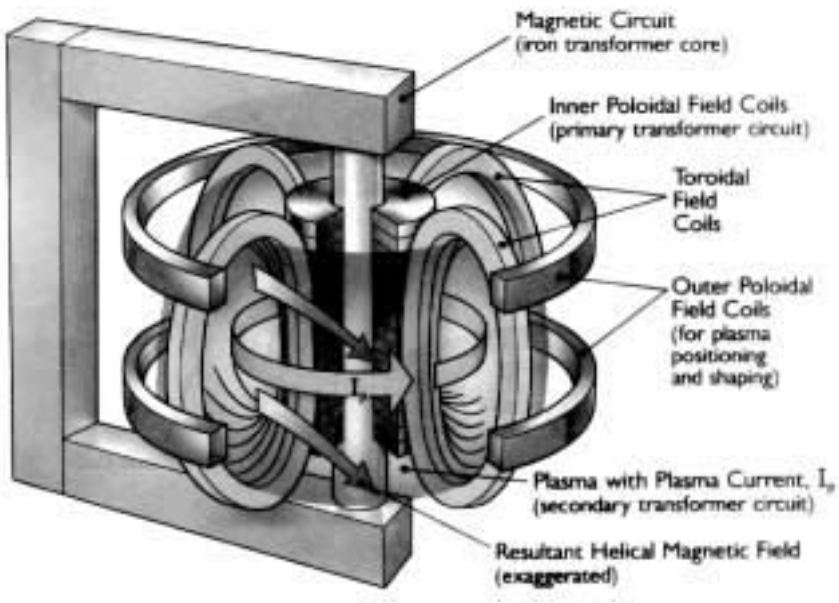

Fig. 1.1. *A standard tokamak [1]. The magnetic circuit is the core of the transformer; the poloidal field coils are the primary circuit; the plasma forms the secondary.*

The efficiency of the confinement is expressed by the parameter β, defined as the ratio of the average plasma energy to the average magnetic energy.

The principal magnetic field is generated by external coils along the longitudinal (or *toroidal*) direction. However, in order to provide plasma equilibrium and stability, it is necessary also to have a component of the magnetic field in the transversal (or *poloidal*) direction. This poloidal component is produced mainly by a toroidal current in the plasma itself. The superposition of the toroidal and poloidal magnetic fields results in helical magnetic field lines. A measure of the pitch of a field line is given by the *safety factor*, q, equal to the number of toroidal passes necessary to complete one pass in the poloidal direction.

The toroidal plasma current is usually induced by transformer action, where the plasma plays the role of the secondary circuit.

The magnetic field makes possible the plasma confinement by holding the charged particles into small gyrating orbits. By this means the ions are forced to travel a distance a million times the dimensions of the vessel before reaching the wall.

In a reactor the continuous power losses should be replaced by a sufficiently large thermonuclear power. This requires that a sufficiently hot plasma be stably confined at a high enough density for a sufficiently long time. The best figure of merit to assess the approach to reactor condition is therefore the triple product $n\tau_E T$, where n is the plasma number density, τ_E is the energy confinement time and T is the fuel temperature. The minimum value of $n\tau_E T$ required for net power production is achieved for the most reactive fuel of D and T at the optimized temperature $T \gg 15$ KeV ($\gg$ 170 million °C) and is about $5 \cdot 10^{21} \mathrm{m}^{-3}$ s keV [1].

Another important figure of merit is Q, defined as the ratio of the fusion power to the external heating power supplied to maintain the plasma temperature. At $Q = 1$ the fusion power generated in the plasma equals the heating power supplied ("breakeven" condition). For Q_{fi} ¥ the power generated in the plasma is sufficient to sustain the fusion reactions, with no need to supply external heating ("ignition" condition).

Figure 1.2 shows recent achievements in the simultaneous values of n, τ_E, T, by some of the largest tokamaks in the world. The figure shows that for several tokamaks the triple product is close to the breakeven requirement, and less than a factor of ten away from the goal of fusion ignition. Recently, researchers from the JT-60U tokamak in Japan reported high-confinement discharges having a triple product exceeding breakeven conditions [2].

Assuming that the goal of ignition is achieved, to be economically attractive a fusion power source will need to operate at high values of the parameter β, since the average fusion power density can be shown to scale as $\beta^2 B_f^4$ [3], and B_f, the toroidal field on axis, is limited by technological factors of magnet design. As β increases, the size and initial cost of the fusion power source can be reduced. Unfortunately, a violent type of instability

poses severe constraints to the maximum achievable b ina tokamak. This instability and a possible cure for it are outlined in the following section.

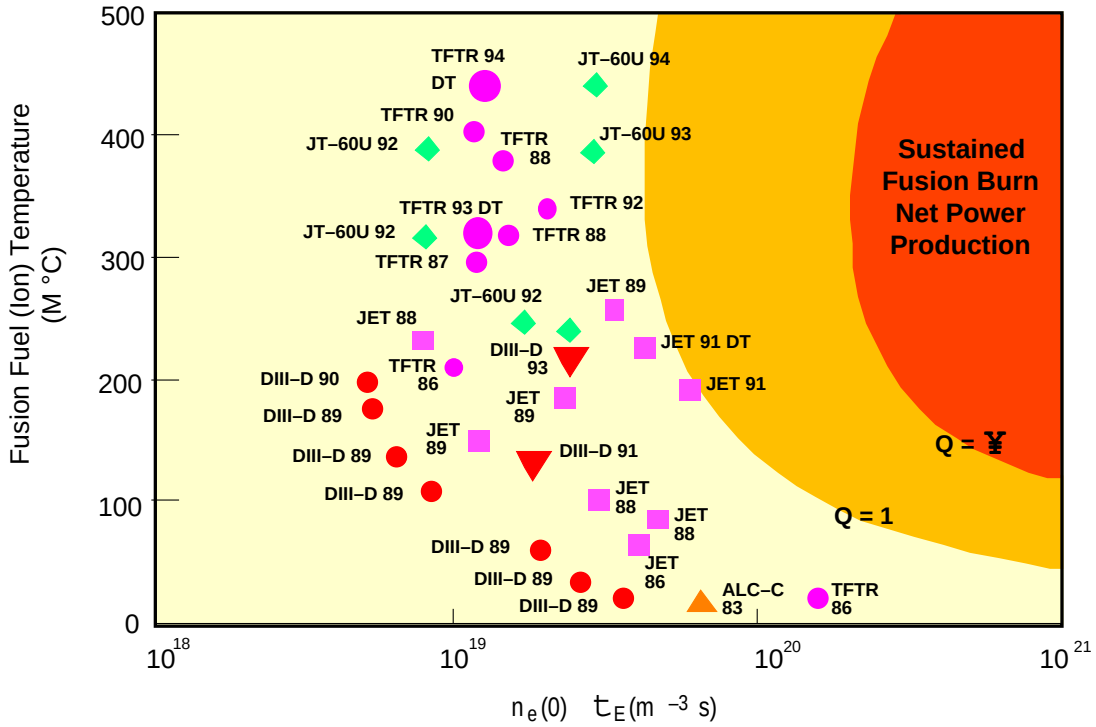

Fig. 1.2. *Central ion temperature versus confinement quality (number of particles per cubic meter confined for one second), for a selected number of representative tokamaks worldwide in the period 1983-1994 [4].*

1.2. MHD and the Importance of Wall Studies

The simplest available mathematical model that is able to accurately describe the macroscopic equilibrium and stability properties of a plasma is the ideal magneto hydrodynamic theory. The theory describes how inertial, magnetic and pressure forces interact within a perfectly conducting plasma. When stability limits set by ideal MHD are violated, usually a catastrophic termination of the plasma discharge on a very short time scale is the consequence. A simple classification of MHD instabilities can be made

neglecting the effects of toroidicity in a circular cross section tokamak ("straight" tokamak) [5, 6].

The potentially strongest instability is the *external kink mode*, destabilized by the gradient of the toroidal plasma current. In the straight tokamak the ideal hydromagnetic kink can occur only if a vacuum region surrounds the plasma, because the instability entails the deformation of the plasma surface into a helix. This perturbed helix is described by the toroidal and poloidal mode numbers, n and m, representing respectively the number of wavelengths contained in one period of the toroidal and poloidal angles.

The $m = 1$ *internal kink* is a special case of kink instability, which can exist as a purely internal mode, i.e. not affecting the equilibrium position of the plasma-vacuum boundary.

The other general type of instability that is found is the *interchange instability*. In this case the perturbed magnetic surface is in the form of flutes along the magnetic field lines. Typically these modes have growth rates that are slower than the kink modes by a factor equal to the inverse aspect ratio, ϵ (the aspect ratio is defined as the ratio of the major radius of the plasma, R, to the minor radius, a). This instability is purely internal and is destabilized by the gradient of the pressure.

The assumption of ideal (i.e. perfectly conducting) plasma constrains the magnetic field structure to a fixed topology. The presence of resistivity eliminates this constraint and can introduce instability to configurations that were ideally stable against interchange and kink modes. The linear growth rate for resistive instabilities has a fractional power dependence on the plasma resistivity.

When toroidal effects are included, a new type of ideal instability, the *ballooning modes*, is introduced. Like interchanges, ballooning modes are internal pressure driven instabilities. These modes, however, are not constant along a field line and are concentrated in regions where the magnetic field lines have curvature that is unfavorable for stability, i.e. where the field lines are concave to the plasma (outer side of the torus). For a given ratio of plasma current to magnetic field, ballooning modes set a maximum value of β achievable

in the “first region of stability” of a tokamak [7]. For a wide class of equilibria, however, these modes can be restabilized at higher values of β, in the “second stability regime” [8].

The most important effect of toroidicity, however, is the appearance of ballooning of long wavelength modes across magnetic surfaces and the pressure destabilization of the external kink. This *external ballooning-kink instability* usually sets the most severe limit on beta in a conventional tokamak, a limit that is rather well reproduced by the simple scaling law [9]:

$$\textit{normalized beta } (\beta_N) = \frac{\beta(\%)}{I_p / aB_t} \leq 2.8$$

where the plasma current, I_p, is measured in mega-amperes, a in meters and B_t in teslas.

Since an external mode requires motion of the plasma-vacuum interface away from its equilibrium position, the ideal recourse to overcome such instability would be to place a perfectly conducting wall, also referred to as a shell, surrounding the plasma and close to its surface (in this thesis we shall use the terms wall and shell interchangeably to refer to the conducting structure used to stabilize the external kink mode). In this way the eddy currents generated in the wall by the plasma displacement can react back on the mode and neutralize it.

Almost all *advanced tokamak* regimes, defined as plasma equilibria having high beta, high energy confinement time and high “bootstrap” current (non-inductive, self-generated toroidal plasma current, favorable for steady state operation), rely on a close fitting perfectly conducting wall to stabilize the $n = 1$ external ballooning-kink mode. This is the case of advanced regimes calculated for TPX [10] (proposal for a compact, high β_N, steady state tokamak), NSTX [11] (ultra-low aspect ratio device, to be built in Princeton), ARIES-II and ARIES-IV [12] (studies for tokamak power reactors), DIII-D [13] (tokamak capable of the highest stable values of β_N), JET [14] (world’s largest tokamak, operating in England).

In addition, sensitivity studies on safety factor profiles for conventional operating modes in ITER, world’s largest international collaboration for an ignition experiment

(presently under design), have found coupled internal-external kink modes unstable at very low beta values [15]. These modes can be stabilized by a perfectly conducting wall.

Due to finite dissipation in any real wall, for non-rotating plasmas the eddy currents can only slow down the instabilities to the order of a characteristic penetration time of the wall. In this case the modes are usually called *wall modes*, and their slow growth rates may allow feedback techniques to provide stabilization [6, 16-18].

Recently, theories [19-21] and computations [22] that included some form of dissipation in the model for the plasma, suggested that a resistive wall can act like a perfectly conducting wall in the presence of sufficiently rapid plasma rotation. Experimental results in DIII-D [23] and PBX-M [24] have found possible explanation in these resistive wall mode theories.

These theories and the experimental studies, however, are still under development, and are especially limited on the effect of non-uniformity or gaps in the wall [25], which is seen as unavoidable in an actual reactor for access to the plasma of diagnostics and particle beams.

1.3. Wall Stabilization in HBT-EP

The HBT-EP (High Beta Tokamak, Extended Pulse) experiment at Columbia University was designed and built to make possible a systematic study of the effects of a resistive wall on the stability of the kink mode. A fast ohmic heating system and insulating quartz breaks in the stainless steel vacuum chamber enable rapid formation of the plasma discharges in a high-b state that can be sustained for up to about 10 ms. Simulations of HBT-EP with ideal MHD codes, described in Chapter 2, show that the maximum achievable beta values can be beyond the stability limit to external ballooning-kink modes at low values of the edge safety factor, for typical equilibria. The internal conducting wall is segmented so that it can be moved independently from the surface of the plasma, allowing

us to vary the plasma-wall distance and the symmetry and extension of the coverage, while keeping the other plasma parameters nearly identical.

In addition, currently under investigation is the use of a system of coils, installed outside the vacuum chamber in correspondence of the quartz gaps, to apply magnetic perturbations in such a way to control the toroidal rotation or the amplitude of an unstable mode [26], once the growth rate of the instability has been slowed down by the wall.

Since the first high beta operation, reported in 1993 [27], experimental studies of passive control of MHD instabilities have already shown systematic improvement of plasma stability as the wall is gradually moved closer to the plasma surface [28, 29].

1.4. Thesis Objective

The goal of this thesis is to improve our understanding of the interaction of a segmented, resistive wall with hydromagnetic external kink instabilities. To achieve this goal the thesis focuses on the examination of the eddy current patterns induced on the internal wall by MHD instabilities during wall stabilization experiments. Accurate equilibrium reconstructions have enabled us to compare the experimental observations with the predictions of ideal MHD theory. The similarities and differences between the patterns on the actual and on a model, continuous wall, provide important information on the wall-stabilization mechanism when a thick and segmented wall is used. This knowledge can provide valuable guidance for the construction of an active feedback system and for effective, yet economical, design of passive conductors in new machines.

1.5. Thesis Outline

The continuation of this thesis is organized as follows: Chapter 2 reviews the ideal MHD theory of wall stabilization and introduces the numerical codes used for the equilibrium and stability modeling; Chapter 3 describes briefly the HBT-EP tokamak and some of its diagnostics; Chapter 4 describes the equilibrium reconstruction procedure;

Chapter 5 presents the experimental measurements in comparison with the numerical predictions; Chapter 6 concludes with a discussion of the results.

2

Ideal MHD Modeling

2.1. Introduction

In ideal MHD ions and electrons do not appear as separate identities, but are treated as a single perfectly conducting fluid. The basic requirement for this treatment to be valid is that the plasma be collision dominated. At the same time there should not be too many collisions or else the plasma will be dominated by resistive diffusion. The phenomena that can be described are those with length scale of the order of the overall plasma dimension, and characteristic speed which is the thermal velocity of the ions. For HBT-EP, with a length scale of 0.2 m and deuterium ions at T = 100 eV, this gives a characteristic time $t_{MHD} \gg 2$ ms.

Two important further approximations needed for the model are that the inertia of the electrons is neglected, and that high frequency information is ignored, which also leads to the assumption of local quasi-neutrality in the plasma ($n_i \gg n_e = n$).

When the approximations described above are introduced in the full set of Maxwell's equations coupled with fluid equations for electrons and ions, one attains the following model for a plasma, in MKS units [6]:

$$\frac{\partial \rho}{\partial t} + \quad \rho \mathbf{v} = 0$$

(mass conservation),

$$\rho \frac{\partial \mathbf{v}}{\partial t} + \rho(\mathbf{v} \quad)\mathbf{v} = \mathbf{J} \cdot \mathbf{B} - \quad p$$

(momentum conservation, assuming scalar pressure),

$$\cdot \mathbf{E} = -\frac{\partial \mathbf{B}}{\partial t}$$

$$\cdot \mathbf{B} = \mu_0 \mathbf{J} \qquad (2.1)$$

$$\mathbf{B} = 0$$

(Maxwell's equations),

$$\mathbf{E} + \mathbf{v} \cdot \mathbf{B} = 0$$

(Ohm's law),

$$\left(\frac{\partial}{\partial t} + \mathbf{v} \right) \left(\frac{p}{\rho^{\gamma}} \right) = 0$$

(energy conservation, with γ = 5/3 for adiabatic law), where the unknowns are density, pressure and the three components of magnetic field, electric field, current density and fluid velocity, fourteen in all.

2.2. MHD Equilibrium

By reducing the time independent ideal MHD equations for the case of toroidal axisymmetry and zero fluid velocity, one obtains a two-dimensional, nonlinear, elliptic partial differential equation known as the Grad-Shafranov equation [30]:

$$R \frac{\partial}{\partial R} \left(\frac{1}{R} \frac{\partial \psi}{\partial R} \right) + \frac{\partial^2 \psi}{\partial Z^2} = -\mu_0 R^2 \frac{dp}{d\psi} - F \frac{dF}{d\psi} \qquad (2.2)$$

where ψ is proportional to the poloidal flux in the plasma and $F(\psi) = RB_{\phi}$.

The TokaMac code [31] has been used in this thesis to find, numerically, free-boundary solutions of equation (2.2) either for prescribed functions $p(\psi)$ and $F(\psi)$, or subject to the constraints imposed by experimental measurements.

The code first uses Green's functions to calculate, over an up-down symmetric computational domain, the values of the poloidal flux due to the external coil currents and an initial guess of the plasma current, then iterates on the solving of (2.2) followed by a recalculation of the flux.

The solution of (2.2) is accomplished using finite elements and, when fitting to experimental measurements, following the method of Lao, *et al.* [32]: a least square procedure calculates the coefficients in polynomial expansions of the functions $p(\psi)$ and $F(\psi)$ that produce the best fit of the calculated quantities to the experimental measurements. Alternatively, one can prescribe the profile shape for the functions $p(\psi)$ and $F(\psi)$.

2.3. MHD Stability

One way to test the stability of the calculated equilibria is to linearize all quantities about the equilibrium state, express the time dependence of the perturbed part as $\exp(-i\omega t)$ and substitute in the MHD equations; one finds the equation that represents the normal-mode formulation of the problem of linear MHD stability of a plasma:

$$-\omega^2 \rho \xi = F(\xi) \qquad (2.3)$$

where $F(\xi) = \frac{1}{\mu_0}(\nabla \times \mathbf{Q}) \times \mathbf{B} + \frac{1}{\mu_0}(\nabla \times \mathbf{B}) \times \mathbf{Q} + \nabla(\xi \cdot \nabla p + \gamma p \nabla \cdot \xi)$ is the force operator, ξ is the displacement vector and $\mathbf{Q}$ is the perturbed magnetic field.

The energy principle [33] provides a method for answering the question of stability which does not require the determination of the eigenvalues and eigenfunctions.

In the extended energy principle [33,34] an equilibrium is exponentially stable if and only if the change in potential energy satisfies

$$\delta W = \delta W_F + \delta W_S + \delta W_V \neq 0 \qquad (2.4)$$

for all allowable perturbations, with fluid, surface and vacuum contribution to δW given by [35, 36]:

$$\delta W_F = \frac{1}{2}\int_P d\mathbf{r}\left[\frac{|\mathbf{Q}_\perp|^2}{m_0} + \frac{B^2}{m_0}\left|\xi_\perp' + 2\xi_\perp \kappa\right|^2 + \right.$$
$$\left. + \gamma p\left|\nabla\cdot\boldsymbol{\xi}\right|^2 - 2(\xi_\perp\cdot\nabla p)(\kappa\cdot\boldsymbol{\xi}_\perp^*) - J_{//}(\boldsymbol{\xi}_\perp^*\times\mathbf{b})\cdot\mathbf{Q}_\perp\right],$$

$$\delta W_S = \frac{1}{2}\int_S dS\left|\mathbf{n}\cdot\boldsymbol{\xi}_\perp\right|^2\mathbf{n}\cdot\left[\!\left[p+\frac{B^2}{2m_0}\right]\!\right], \qquad (2.5)$$

$$\delta W_V = \frac{1}{2}\int_S d\mathbf{r}\frac{\left|\hat{\mathbf{B}}_1\right|^2}{2m_0},$$

where $\hat{\mathbf{B}}_1$ is the perturbed magnetic field in the vacuum, κ is the normal curvature of the magnetic field and the subscripts $\perp$ and // designate directions perpendicular and parallel to the equilibrium magnetic field.

The first and second terms in δW_F represent the energy required to, respectively, bend and compress the magnetic field lines. The third term represents the energy required to compress the plasma. These first three terms are positive definite and therefore always stabilizing. The fourth and fifth terms can be negative and thus drive instabilities. They represent the destabilizing effect of, respectively, the pressure gradient and the plasma current component parallel to the magnetic field.

The surface contribution, δW_S, is zero if there are no surface currents. The vacuum contribution, δW_V, is positive definite and therefore always stabilizing.

2.3.1 Analytic Model

As a point of reference let's consider the stability to ideal MHD external kink in the simple "straight tokamak" case of Fig. 2.1, i.e. a cylindrical plasma of length $2\pi R_0$, with circular cross section of radius a, in which the fields satisfy the ohmically heated tokamak expansion [6]:

$$B_\theta / B_z \sim \varepsilon,\ k_{//} a \sim \varepsilon,\ \beta_t \sim \varepsilon^2. \qquad (2.6)$$

Here $\varepsilon = a/R_0$ is the inverse aspect ratio and k is the wave vector.

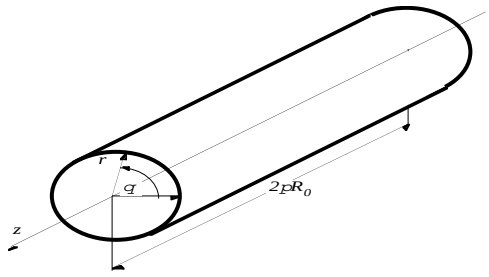

Fig. 2.1. *Geometry of the "straight" tokamak.*

The perturbation, that we assume has a resonance surface outside the plasma, can be Fourier analyzed in the θ and z coordinates:

$$\xi(\mathbf{r}) = \xi(r) \exp i(m\theta + kz - \omega t). \qquad (2.7)$$

Assuming that no surface current flows on the plasma, the change in the potential energy is:

$$\delta W_b = \delta W_F + \delta W_{Vb} \qquad (2.8)$$

with a perfectly conducting wall at radius $b>a$, and

$$\delta W_\infty = \delta W_F + \delta W_{V\infty} \qquad (2.9)$$

with the wall at infinity.

If the same perturbation $x(\mathbf{r})$ is considered in (2.8) and (2.9), the values of δW_F are identical with or without the wall, and the effect of the eddy currents is entirely contained in the vacuum contribution, δW_V. From Ref. [37] we have:

$$\delta W_{Vb} = \frac{2\pi^2 R_0 a^2 x_a^2 F^2(a)}{m_0|m|}\Lambda_b \qquad (2.10)$$

and

$$\delta W_{V\infty} = \frac{2\pi^2 R_0 a^2 x_a^2 F^2(a)}{m_0|m|}\Lambda_\infty, \qquad (2.11)$$

where

$F = \mathbf{k}\cdot\mathbf{B}$,

$$\Lambda_b = -\frac{|m|K_a}{kaK_a'}\frac{1-(K_b'I_a)/(I_b'K_a)}{1-(K_b'I_a')/(I_b'K_a')}, \qquad (2.12)$$

$$\Lambda_\infty = -\frac{|m|K_a}{kaK_a'},$$

and $K_z = K_m(kz)$ and $I_z = I_m(kz)$ are modified Bessel functions.

Using $ka \gg kb \sim \epsilon$ we have $\Lambda_b \gg \frac{1+W}{1-W}$, with $W = (a/b)^{2|m|}$, and $\Lambda_\infty \gg 1$, so that the quantity

$$\frac{\delta W_{Vb}}{\delta W_{V\infty}} \gg \frac{1+W}{1-W} \qquad (2.13)$$

can be easily plotted as a function of *m*:.

Figure 2.2 shows the dependence of equation 2.13 on *a/b* for *m* = 3 and on *m* for *a/b* = 15/16, the latter being the ratio appropriate for HBT-EP in the configuration with the wall fully inserted (se Chapter 3).

Note that for a toroidal mode number *n* = 1, *m* corresponds to the *q* value at the flux surface resonant with the external kink. Therefore Fig. 2.2(a) shows that wall stabilization of the *n* = 1 external kink can be very effective at low values of the edge safety factor.

Figure 2.2(b) shows that the stabilizing effect of the wall drops very quickly as the plasma-wall separation increases, and is almost null already at a separation » 0.3a.

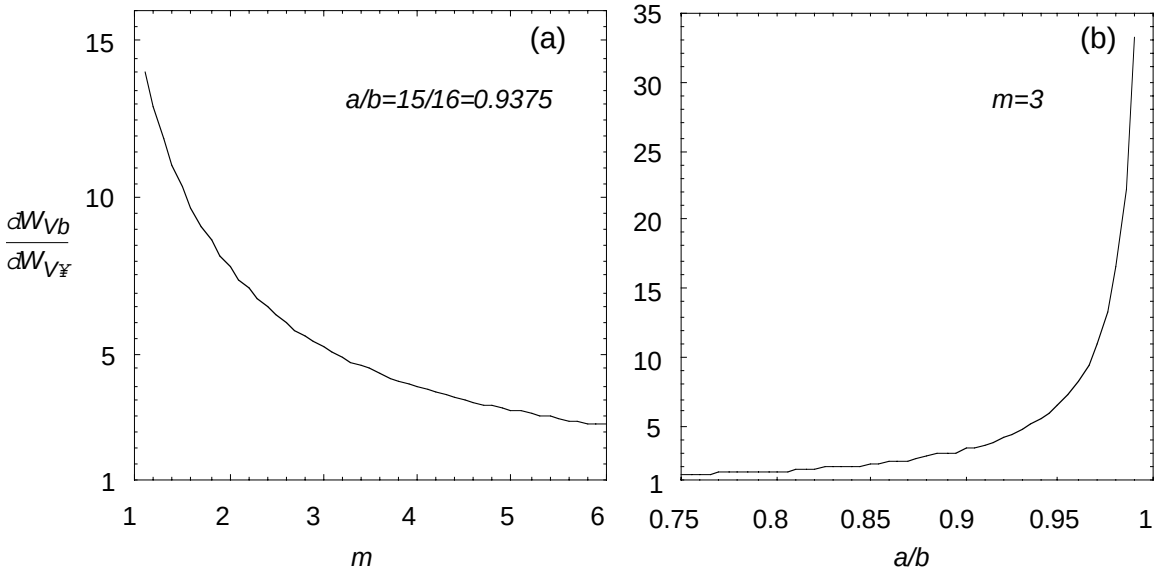

Fig. 2.2. *Plots of* $\delta W_{Vb}/\delta W_{V\infty} \propto (1+W)/(1-W)$, *with* $W = (a/b)^{2m}$. *(a) Versus m with a=15 cm and b=16 cm; (b) versus a/b with m=3. The presence of the wall at b is shown to increase substantially the stabilizing vacuum contribution to* δW *at lower m values, with respect to the no wall case.*

Intuitively, the curves of Fig. 2.2 can be understood by observing that the perturbed magnetic field in the vacuum, between the resonant *q* surface and the conducting wall, is approximately proportional to m/r^{m+1} [5]. As a consequence, for a given amplitude of the perturbation at the resonant surface, the perturbed field at the wall is smaller the larger is *m*

and the farther is the wall. In correspondence to a smaller perturbed field at the wall the perturbed eddy currents are smaller, hence the wall is less stabilizing.

2.3.2 Numerical Solution

If one includes toroidal effects, arbitrary plasma and wall cross section and arbitrary current density and pressure profiles, an analogous analytical treatment is impossible. However, detailed studies can be done using 2D numerical codes such as the Princeton Equilibrium, Stability and Transport (PEST) [38, 39] package of routines that have been used in this thesis.

The PEST1 code [38] solves the linearized ideal MHD equations by extremizing the Lagrangian $L = \omega^2 K(\xi^*, \xi) - \delta W(\xi^*, \xi)$ for small perturbations ξ about the equilibrium state [33]. Here K is the kinetic energy functional and δW is the change in potential energy. Using the practical Galerkin approach, the perturbations are represented by a finite subset of a complete set of functions, $\xi = \sum_{m=1}^{M} a_m^{(M)} \boldsymbol{\psi}_m$. Then, after substitution in the Lagrangian, the volume integral of the error $\varepsilon = L\xi - L^{(M)} \sum_{m=1}^{M} \xi_m$ weighed with the functions $\boldsymbol{\psi}_i$, is set to zero:

$$\int_W \varepsilon \boldsymbol{\psi}_i \, dW = 0 \qquad (2.14)$$

If ξ is a solution of the linearized ideal MHD equations then L=0, and (2.14) reduces to:

$$\sum_{m=1}^{M} \left(\int_W \boldsymbol{\psi}_i \, \delta W^{(M)} \boldsymbol{\psi}_m \, dW - \int_W \boldsymbol{\psi}_i \omega^{(M)2} K^{(M)} \boldsymbol{\psi}_m \, dW \right) a_m^{(M)} = 0. \qquad (2.15)$$

This is a matrix eigenvalue problem whose solution yields approximations $\omega^{(M)2}$, $a_m^{(M)}$, to ω^2 and a_m. The vector nature of the $\boldsymbol{\psi}$'s is denoted symbolically; actually the different vector components must be treated independently.

In the non orthogonal PEST coordinate system an appropriate flux label $\psi = \psi(\Psi)$ is chosen to represent the radial variation, and the poloidal (θ) and toroidal (ζ) angle coordinates are chosen so that the field lines are straight on each surface. Each of the three components of the vector $\mathbf{x}$ is then expanded in a combination of finite elements, to represent variation normal to the magnetic surfaces, and Fourier series, for behavior in them, e.g.:

$$x_\psi(\psi,\theta,\zeta) = \sum_{l,m} x_{l,m,n} u_m(\psi) \exp i(l\theta - n\zeta). \qquad (2.16)$$

The allowable perturbations are those for which the displacement has a finite kinetic energy norm and the perpendicular component of the perturbed magnetic field is continuous at the plasma-vacuum interface and vanishes at the perfectly conducting wall. The plasma-wall distance is a fixed multiple of the minor radius, and can be extended to "infinity".

For more flexibility in the modeling of the wall one can use the code VACUUM [40] to supply the correct vacuum contribution to δW. The code is capable of handling a generic dee shaped wall, toroidally symmetric, with one poloidal gap and a deformable bulge on the outer midplane. If an instability is found, VACUUM interfaced with PEST1 can calculate and display the eddy current pattern induced by the instability on the conducting wall.

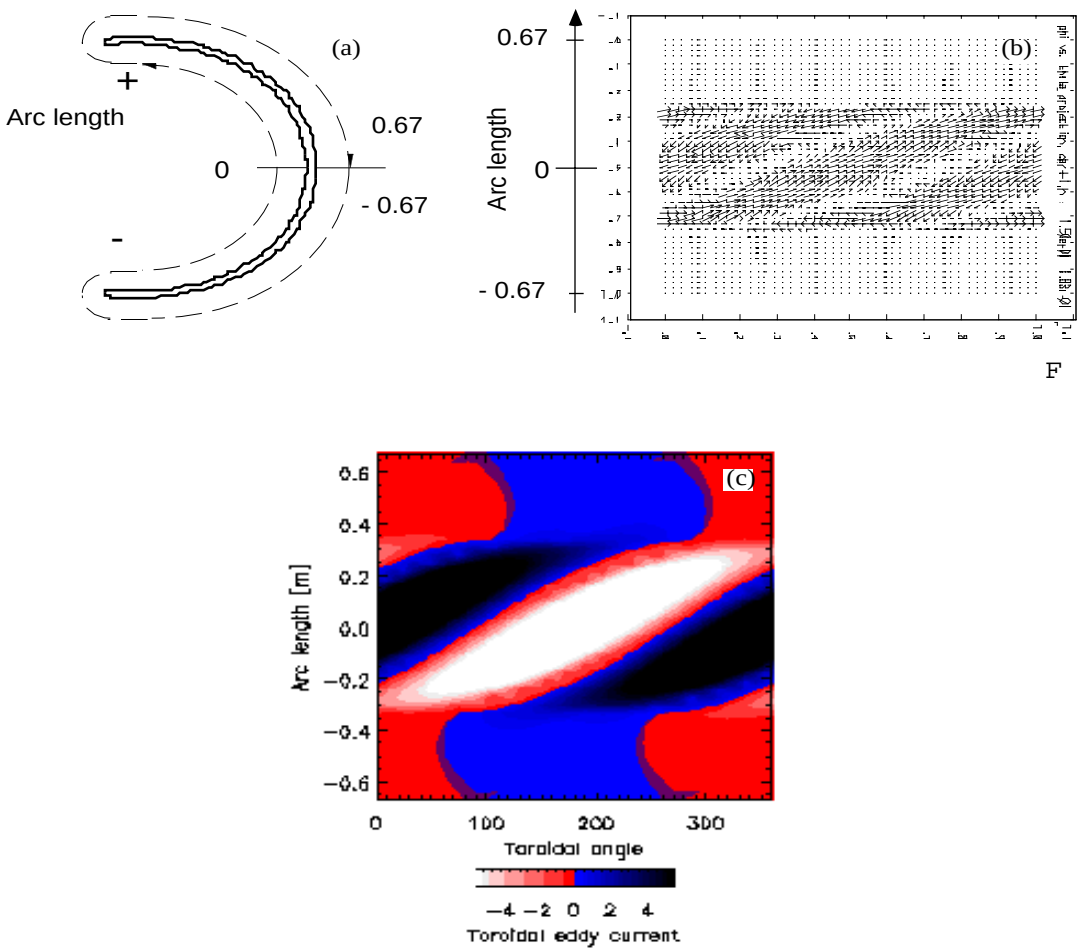

Fig. 2.3. *A VACUUM type of external conductor (a) and the calculated instability-induced eddy current in the "poloidal arc length-toroidal angle" plane: (b) arrow plot and (c) toroidal component .*

In PEST2 [39] the three component normal mode equations are reduced to that involving only the component $x_y = x \quad y$ of the plasma displacement. This is achieved by minimizing the potential energy with respect to the other two components and using a model kinetic energy $K_{//} = w^2 \; r|x \quad y|^2 dt/2$. Physically, the model kinetic energy normalization restricts the nonaxisymmetric perturbations to incompressible modes.

The code is faster and more accurate than PEST1 and therefore preferable when one is interested in the determination of marginal stability and not in the exact growth rates and eigenfunctions.

2.4. MHD Stability in HBT-EP (Model Profiles)

A systematic study of plasma stability to ideal MHD external kinks for model current and pressure profiles in HBT-EP was carried out using the PEST2-VACUUM codes. The effects on stability of wall position, magnetic shear and pressure profile shape have been investigated varying only a single element in parameter space at a time.

Using the TokaMac code to generate the equilibria used in the study, the pressure distributions are given by the relation

$$P' = P_0 (1 - X)^{(\gamma - 1)}, \qquad (2.17)$$

where the derivative is intended with respect to $X = \frac{\psi - \psi_0}{\psi_{lim} - \psi_0}$, and ψ_{lim} and ψ_0 are respectively the poloidal flux at the plasma boundary and at the magnetic axis. The parameter P_0 is adjusted to give the desired value of β; the parameter γ allows for the choice among more or less peaked pressure profiles, as shown in Fig. 2.4(a).

An expression analogous to (2.17) is used to parametrize the derivative of the square of the function $F(\psi)$.

The safety factor q is assumed always increasing monotonically from just above 1.0 at the magnetic axis to values between 1.7 and 6.4 at the boundary [Fig. 2.4(b)], except for the case in Fig. 2.7, where q on axis is 1.1.

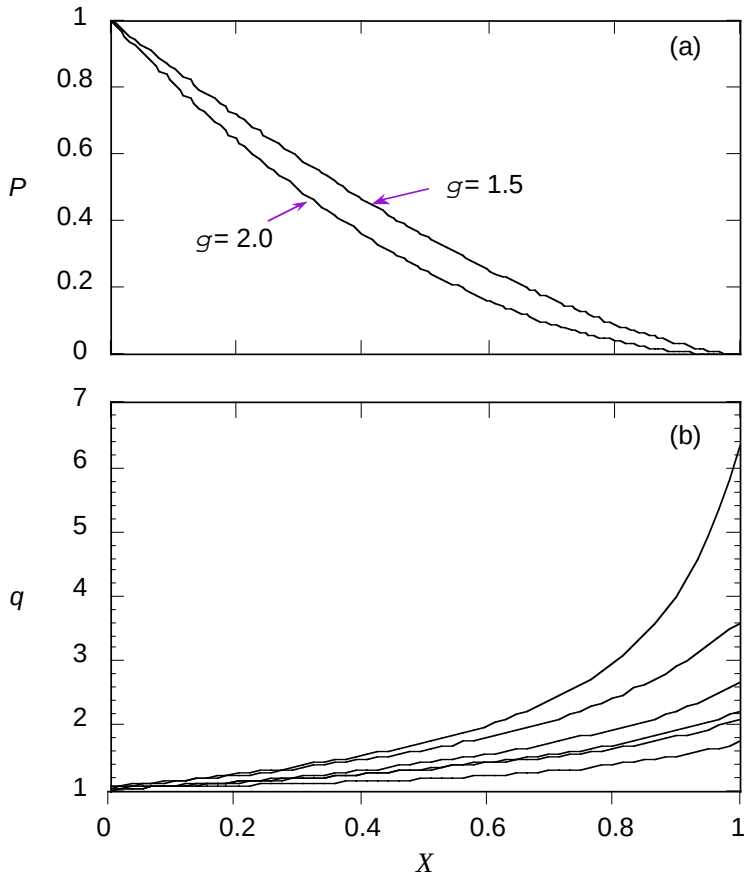

Fig. 2.4. *Sample profiles plotted against* $X = (\gamma - \gamma_0)/(\gamma_{lim} - \gamma_0)$ *used in the stability calculations; (a) pressure profiles for the parameters* g *= 1.5 and 2.0 and (b) q profiles for different values of* q_{edge}.

Fig. 2.5 shows the calculated critical normalized beta, β_{Nc} (i.e. the maximum stable β_N), to n = 1 external kink for different wall positions as a function of the edge safety factor, q_{edge}, and for g = 2. The technique described in Ref. [41, 42] has been used to determine the β_{Nc}'s: for each chosen q_{edge}, from an initial equilibrium with the appropriate parameters, we generate a series of flux-conserved equilibria, i.e. equilibria having the same boundary shape, q-profile and shape of pressure profile but increasing β. The critical normalized β is calculated by extrapolating from a set of values of the growth rate versus β_N, for $\beta_N > \beta_{Nc}$.

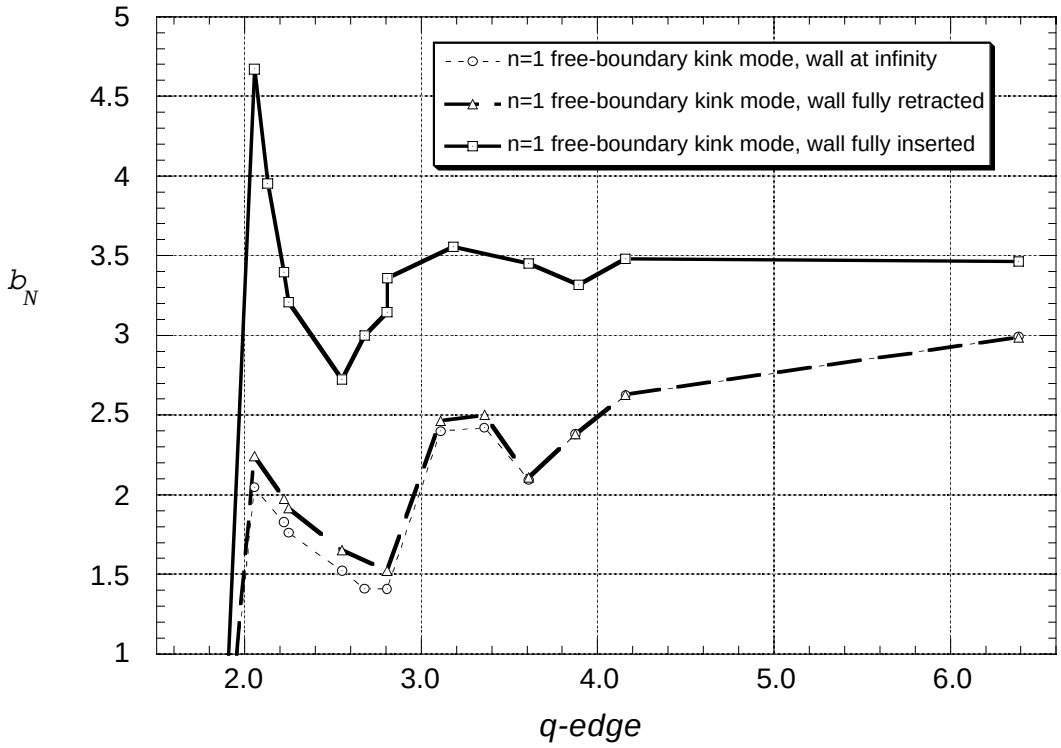

Fig. 2.5. *Effect of plasma-wall separation on the marginal stability boundaries for n = 1 kink, plotted as critical* b_N *versus* q_{edge}*, for monotonic q-profiles increasing from* q_0 *just above 1.0 and parabolic pressure profiles with parameter* g *= 2.0.*

Like in the straight tokamak case, the wall is predicted to have a stabilizing effect increasing at lower q_{edge}. The unstable region is accessible to HBT-EP in the shells fully retracted configuration already at values of $b_N \gg 1.5$, with $q_0 \gg 1.0$

The stability improves when less peaked pressure profiles are used (g = 1.5), as shown in Fig. 2.6 for a smaller range in q_{edge}. The effect is dramatically enhanced in the wall fully inserted configuration. Fig. 2.6(b) shows that the stability limit moves at or beyond values of b_N that are too high for a correct modeling with the available numerical tools.

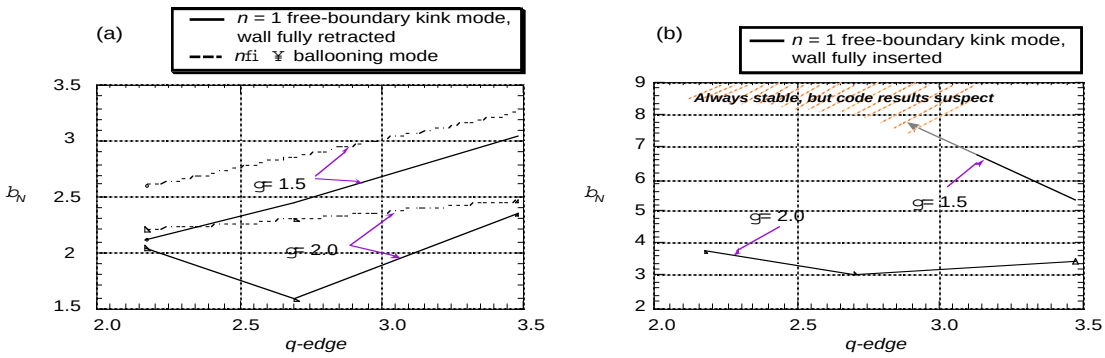

Fig. 2.6. *Effect of pressure profile shape on the marginal stability boundaries to nfi ¥ ballooning and n = 1 kink, plotted as* b_{Nc} *versus* q_{edge} *for* g *= 1.5 and* g *= 2.0 in the configurations (a) wall fully retracted and (b) wall fully inserted (the wall does not affect the ballooning mode).*

In Fig. 2.7 the ideal MHD stability for an equilibrium with parameter g = 1.8 and safety factor profile with q_0 = 1.1 and q_{edge} = 2.8 is examined as a function of the toroidal mode number, *n* for different wall positions. It is calculated that when the shells are fully inserted the ballooning modes become the limiting instabilities. However, it is likely that small modifications of the pressure profile could stabilize these modes.

With respects to the equilibria of Fig. 2.4, the lower b_{Nc} to *n* = 1 kink in the wall fully retracted configuration shows that the destabilizing effect of a higher q_0 is stronger than the stabilizing effect of a flatter pressure profile (lower g). In the wall fully inserted configuration the pressure profile effect is much larger and, combined with the higher q_0, still gives a higher b_{Nc}.

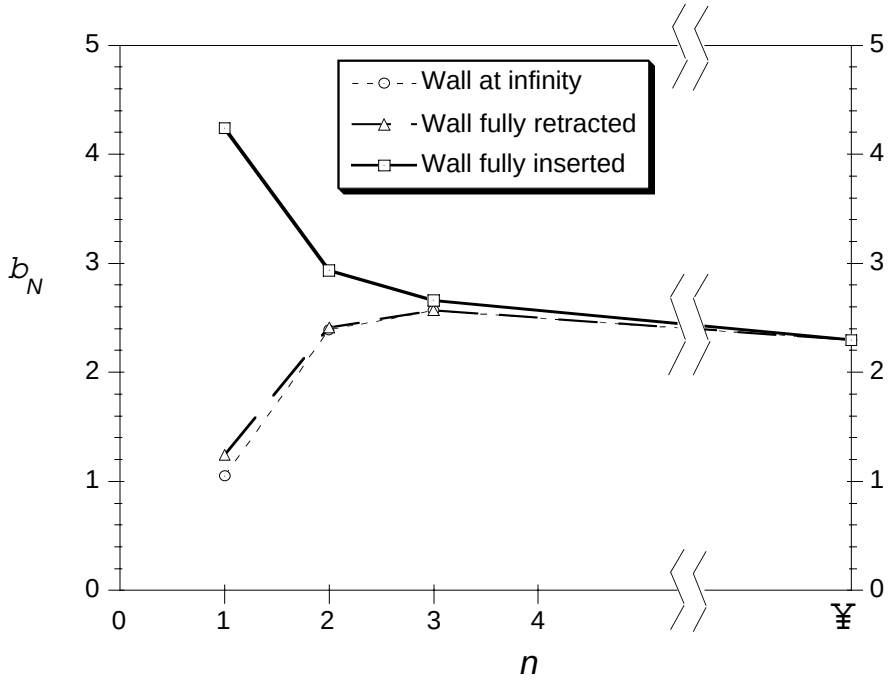

Fig. 2.7. *Effect of plasma-wall separation on ideal MHD marginal stability boundaries, plotted as* b_{Nc} *versus the toroidal mode number n, for pressure profile with parameter* g *= 1.8 and safety factor profile with* q_0 *= 1.1 and* q_{edge} *= 2.8.*

A stability analysis carried out using model profiles is usually very important in the design phase of a new experiment. In the case of HBT-EP the results presented in this chapter have guided us in the preparation of our earlier wall stabilization experiments [29] and were extremely helpful in the interpretation of the results obtained from the experiments.

Much of the work described in the following chapters has been spurred by the willingness to attain a closer-to-real representation of HBT-EP's equilibria, to better understand and interpret the experimental results. Eventually, the marginal stability boundaries plotted in Fig. 2.4 will be confirmed as a good representation of the stability properties of the plasmas in HBT-EP.

3

Experimental Set-Up

3.1. Introduction

This chapter describes briefly the HBT-EP device and some of its diagnostics, with more detail for the ones that have been particularly useful in the work of this thesis. A more thorough description can be found in Ref. [28].

HBT-EP was designed and built to investigate the issues of passive stabilization and active feedback control of low-*n* MHD instabilities, through the use of a close-fitting conducting wall and resonant magnetic perturbations applied by a modular saddle coil system. To contain costs, the design of HBT-EP incorporated the toroidal field coils from the CLEO [43] experiment, and diagnostics from HBT [44], the previous tokamak in the Columbia Plasma Physics Laboratory. Like HBT, also HBT-EP utilizes rapid plasma formation techniques and intense ohmic heating to achieve high beta discharges.

Segmentation of the vacuum chamber and of the internal conducting wall allows fast penetration of the externally applied fields through the toroidal breaks.

Since the first plasma discharge, generated in 1993, HBT-EP has run very reliably. Assembly and disassembly of the machine is relatively simple and diagnostic access very good.

The data acquired by the diagnostics during each shot is digitized in a 10-crate CAMAC system using MIT's MDS software, stored in over 4 GB of on-line storage, optical and tape drives and retrieved for analysis using a cluster of two VAX minicomputers, DEC VAX and Alpha workstations.

3.4. The HBT-EP Tokamak

A schematic top view of the HBT-EP tokamak is shown in Fig. 3.1, where are also indicated the locations of some of its diagnostics.

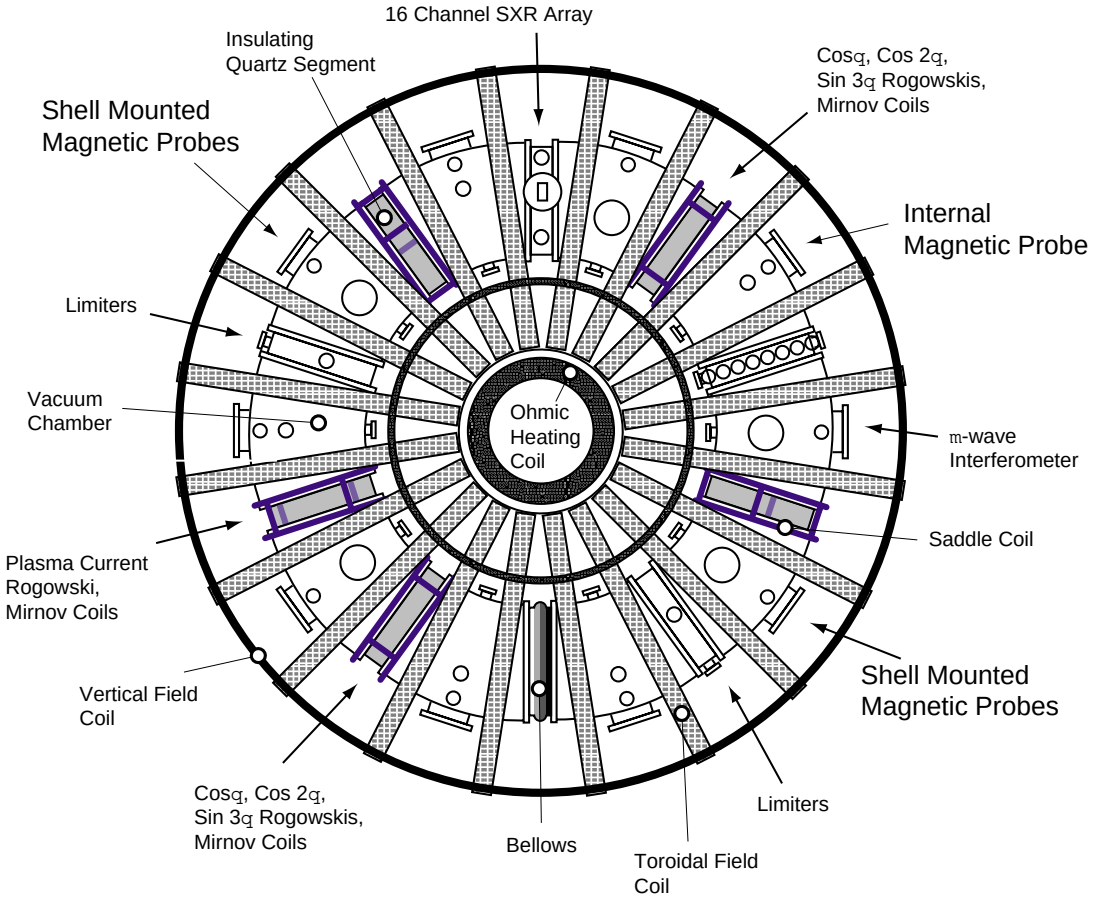

Fig. 3.1. *Schematic top view of HBT-EP.*

HBT-EP's vacuum chamber is composed of ten 20 inch diameter segments, connected together in five locations by quartz cylindrical pieces, in the other five by stainless steel "spool" pieces or bellows. The major radius of the resulting torus is 0.98 m.

All vacuum seals are made either with copper gaskets or double O-rings with inter-ring pumping. Typical base pressure is » 2×10^{-8} Torr.

The twenty toroidal field (TF) coils are powered by a 2 MJ, 10 kV bank with a 100 ms rise time which can generate a maximum of 0.55 T of magnetic field on axis.

The ohmic heating (OH) and the vertical field (VF) coils are also powered by capacitor banks. The current through the OH transformer is initially pre-charged with a negative current having a rise time of about 500 μs. During plasma breakdown, the OH current is driven rapidly to zero within a time of about 50 μs and producing a loop voltage exceeding 300 V. An electron gun provides the initial ionization to help the formation of the plasma current. Typically, the plasma current reaches 18 kA and is sustained for up to about 10 ms by a 1 F electrolytic OH power crowbar. The VF bank, consisting of a fast start followed by a power crowbar, is fired nearly simultaneously with the OH bank.

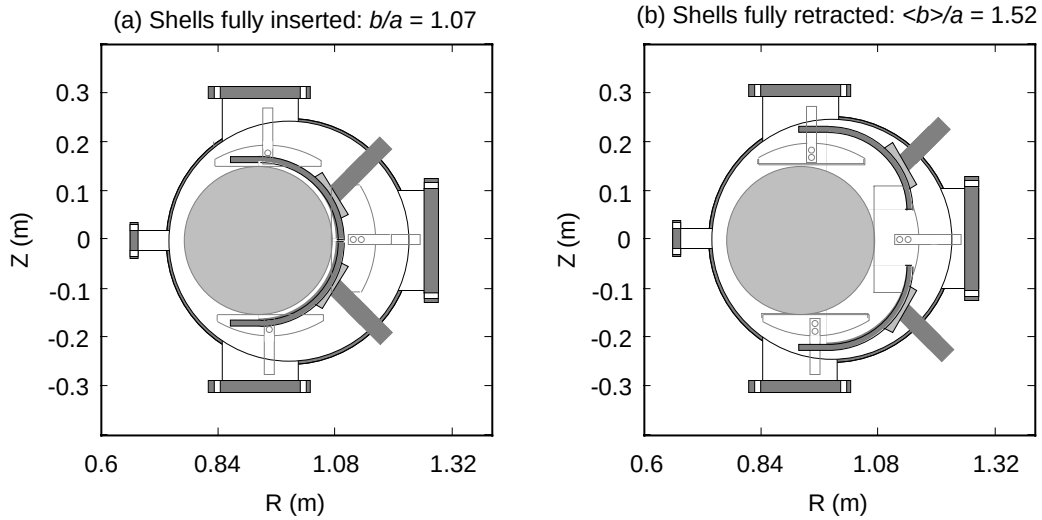

Fig. 3.2. *Simplified cross sections of HBT-EP, showing poloidal limiters and conducting shells in the (a) fully inserted, and (b) fully retracted positions.*

3.2.1 Adjustable Conducting Shells

Figure 3.2 shows simplified cross sections of HBT-EP through one half of the torus in correspondence of one of the toroidal breaks. Each vacuum chamber segment supports a pair of conducting shells. Each shell segment is made of 1.2 cm thick aluminum, nickel plated to minimize sputtering, and can be independently moved in a range of 8 cm along a

radial direction at 45˚ degrees with the outer midplane of the torus. The decay-time of the shell eddy currents, measured during penetration of vacuum vertical field, is $\tau_{L/R} \approx 7.8$ ±1.2 ms [45].

When fully inserted [Fig. 3.2(a)] the shells conform closely to the plasma's outer boundary. In this configuration the plasma minor radius is a = 15 cm and the major radius, $R_0 \approx 92$ cm. The distance of the shells from the plasma surface is about 1 cm (b/a = 1.07), and the toroidal angle covered by each segment is 25˚, for a total coverage of 78% of the outboard surface of the plasma. The toroidal gaps can be thought as comparable to the openings through the wall that in large devices are needed for the access to the plasma by diagnostics and particle beams.

When the shells are fully retracted [Fig. 3.2(b)] the plasma minor radius can be increased to 20 cm by retracting the stainless steel poloidal limiters (one set of them shown in the figure) located in two toroidally opposite spool pieces. Correspondingly the major radius, R_0, varies from 92 to 94 cm. In this configuration the plasma-wall distance varies poloidally, from 9 to ~7 cm ($\langle b \rangle/a$ = 1.52). The numerical calculations discussed in Chapter 2, show that for ideal MHD stability this position is nearly equivalent to having the shells infinitely far from the plasma.

The experiments presented in this thesis are carried out always with the limiters in the fully inserted positions, which give the configurations illustrated in Fig. 3.2.

3.3. Diagnostics

3.3.1 Shell Mounted Probes

At two opposite toroidal locations the shell segments are instrumented with arrays of magnetic coils that measure the magnetic field at the wall in the poloidal and radial directions. Fig. 3.3 shows the configuration of the shell mounted probe array used for the measurements reported in this thesis. The stainless steel boxes on the plasma side of the

wall contain each a pair of coils, for the measurement of $\dot{B}_\theta$ and $\dot{B}_r$. Only $\dot{B}_\theta$ is measured on the outer side of the wall. To date, limited digitizer and amplifier availability has permitted the simultaneous use of only 25 of the 48 coils in this array.

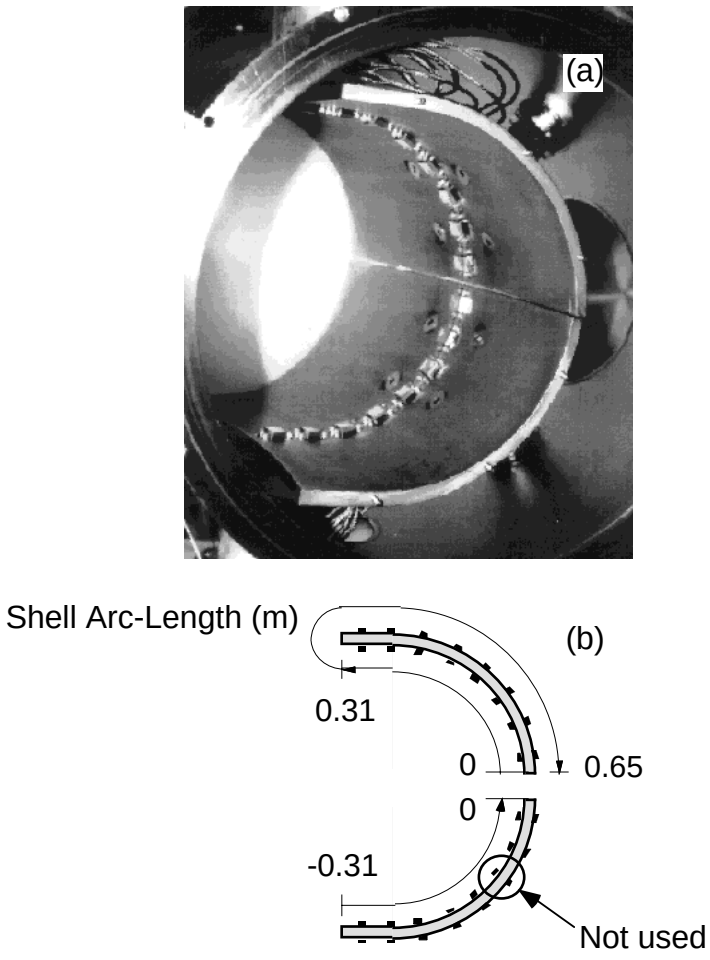

Fig. 3.3. *(a) Photograph and (b) schematic cross-section of the wall segments carrying the Shell Mounted Probe array used in this thesis. The solid boxes represent the stainless steel shields enclosing the Mirnov coils. The coils at the locations circled were shorted to the wall and not used. Shown also is the arc-length convention used in the plotting of the measurements.*

Using a slab approximation, the toroidal component of the current per unit length at the locations between a coil on the plasma facing side (in) and a coil on the vacuum side (out), can be calculated as:

$$k_f = (B_{q,out} - B_{q,in}) / m_0,$$

where the positive sign for k is concordant with the plasma current.

However, due to rotating MHD instabilities, magnetic signals in HBT-EP show fluctuations that usually have frequencies greater than 4 kHz. We then decompose the magnetic signal, B, in a "perturbed" part , dB, and an "equilibrium" part, $\langle B \rangle$, as illustrated in Fig. 3.4. We assume that the perturbed part does not penetrate the wall because the skin depth of aluminum at the above frequencies is only » 1 mm (see Fig. 3.5), much smaller than the thickness of HBT-EP's shells. Therefore from the measurement of dB on each side of the wall we obtain the instability-induced eddy current on each side of the wall:

$$dk_{f,in} = -dB_{q,in} / m_0, \quad dk_{f,out} = dB_{q,out} / m_0.$$

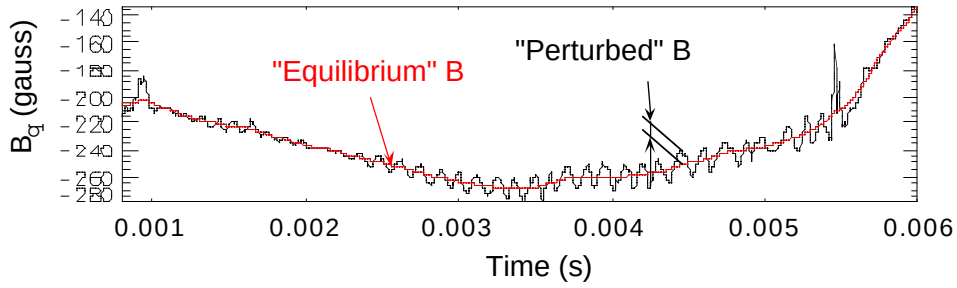

Fig. 3.4. *Example of a shell mounted coil signal, showing the high frequency fluctuations and the decomposition of the signal in "equilibrium" and "perturbed" parts.*

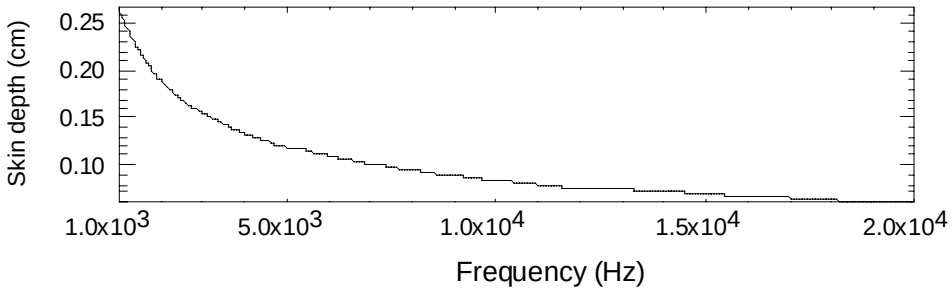

Fig. 3.5. *Skin depth of Aluminum versus frequency of the eddy current.*

3.3.2 Internal Probe

A quartz-encapsulated internal probe array, designed and built for HBT [46], has been mounted on HBT-EP to measure the vertical magnetic field near the plasma edge. The probe was chosen because of its high density distribution of coils up to the probe tip, that permits to measure the poloidal field at a couple of locations inside the plasma without affecting catastrophically the equilibrium. A stainless steel sleeve protects the quartz from localized heat load, which would make the quartz boil off and cool down the plasma edge. To allow radial movement but contain costs, the probe slides trough two dry O-rings with inter-ring pumping. For the experiments in this thesis the tip was always positioned 3 cm beyond the radial limiter edge, toward the plasma axis. Figure 3.6 shows schematically this configuration of the internal probe.

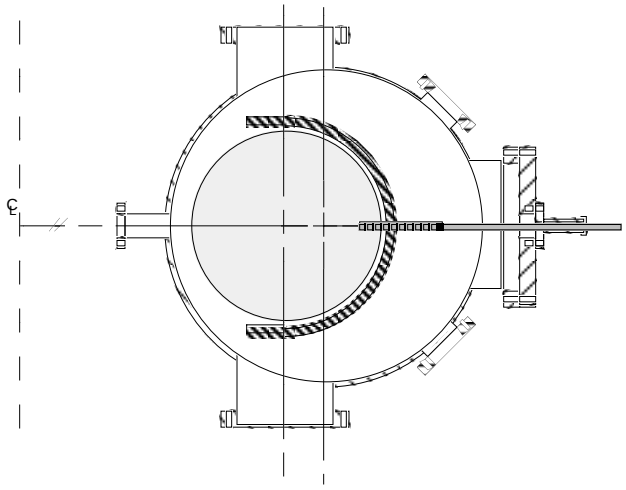

Fig. 3.6. *Configuration of the internal magnetic probe array. The support runs through a hole in the shell segments.*

Other useful magnetic diagnostics include nine poloidal flux loops and Fourier analyzing Rogowski coils mounted on quartz segments and toroidally distributed to identify the parity of the *n* number of the perturbations.

3.3.3 Non-Magnetic Diagnostics

Among non-magnetic diagnostics, this thesis makes use of a microwave interferometer system, to obtain the integrated electron density as a function of time, and of a 16-channel soft x-ray photodiode array, to study the internal structure of the instabilities. Details on this diagnostic can be found in Ref. [47]. Fig. 3.7 shows how the lines of sight of the 16 channels are concentrated through the plasma core.

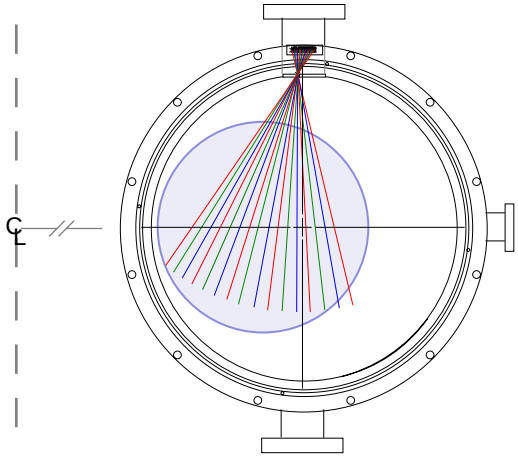

Fig. 3.7. *Soft X-ray array 16-channel map out.*

From the fluctuations in the signals it is possible to estimate the radial plasma displacement in the core [48]. The signal is again decomposed in a perturbed part and an equilibrium part [Fig. 3.8(a)]:

$$S(R,t) = \tilde{S}(R,t) + \langle S(R,t) \rangle$$

For the equilibrium component one can write the Taylor expansion about R_x:

$$\langle S(R,t) \rangle = \langle S(R_x,t) \rangle + (R - R_x)\left.\frac{\partial \langle S \rangle}{\partial R}\right|_{R_x} + \ldots$$

Assuming that the fluctuations $\tilde{S}$ are due to rigid radial displacements, $x = R - R_x$, of the "equilibrium" profile [Fig. 3.8(b)], i.e. $\tilde{S}(R_x,t) = \langle S(R,t) \rangle - \langle S(R_x,t) \rangle$, one obtains:

$$x_r(R_x,t) = \frac{\tilde{S}(R_x,t)}{\left.\frac{\partial \langle S \rangle}{\partial R}\right|_{R_x}}$$

Because heating and transport occur, because the model described is an approximation of reality, and because the SXR signals are chord integrated over the perturbations, usually near the magnetic axis where the denominator goes to zero the value of the fluctuation $\tilde{S}$ does not. To avoid this problem $\tilde{S}$ is decomposed in symmetric and antisymmetric

components with respect to the magnetic axis. Then using only the antisymmetric part restricts us to estimate the radial plasma displacement induced by *m*=odd perturbations.

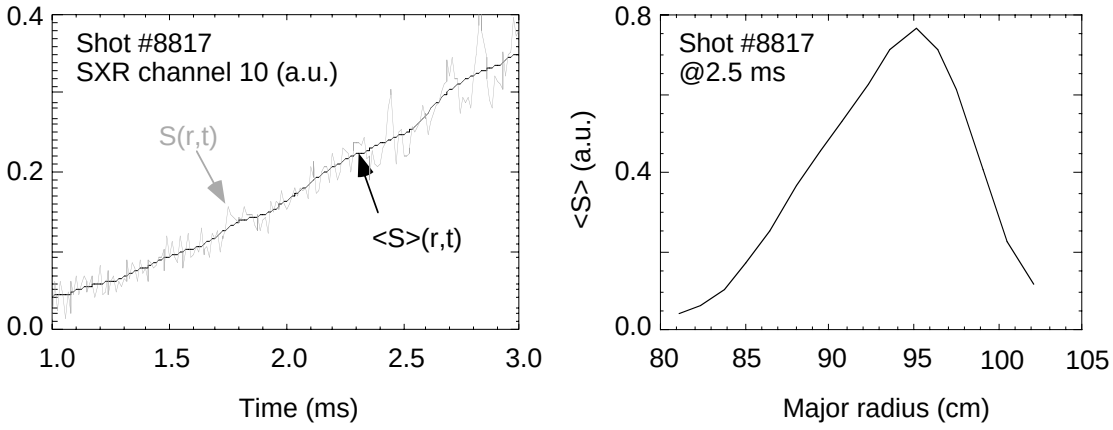

Fig. 3.8. *Examples of (a) SXR signal versus time; (b) profile of the "equilibrium" part of the SXR signal versus the major radius at which the line of sight of each channel crosses the midplane.*

3.5. Machine Operation

It has been shown in Chapter 2 that ideal MHD stability calculations predict low b_N critical to n = 1 external kink for equilibria having peaked pressure profile, low internal inductance and edge safety factor between 2.5 and 3. Therefore, since the object of this thesis are the characteristics of external kink instabilities, the targeted plasma discharges try to meet those requirements.

Our previous wall stabilization experiments have shown destabilization of external kink modes at q_{edge} just below 3 in two types of discharges when the shells are fully retracted: rapid formation and current ramp [29]. The rapid formation technique uses a fast startup, with $\P I_p/\P t \gg$ 100 MA/s, followed by a much slower current ramp. These discharges usually show clear sawtooth oscillations, which enables us to assume in good approximation that $q_0 \gg 1.0$. The destabilization of external kink modes is observed at b_N

values » 1.5, which is in good agreement with the critical value calculated in Fig. 2.5 with a parameter g = 2 for the pressure profile.

The current-ramp type of discharge uses a sustained current ramp of $\P I_p/\P t$ » 6 MA/s, to form plasmas in which the external kink is destabilized at low values of b_N by the low internal inductance. In this case there is often no signal on the SXR diagnostic and there fore no assumption can be made about the value of q_0.

In this thesis we have investigated a third type of discharge, in which characteristics of the previous two discharge types are combined to create plasmas having broad plasma current profile at high b_N. These discharges are created by programming a short period of rapid current startup followed by a moderate current ramp ($\P I_p/\P t$ = 3 MA/s). As the plasma current increases, the vertical field is increased in order to move the magnetic axis away from the outer radial limiter and, thereby, increase the minor radius. This maintains (as much as possible) nearly constant the edge safety factor during the time-period of interest for the stability study.

Because the discharges exhibit sawtoothing oscillations the assumption of $q_0 \gg 1$ can be used in the reconstruction of the equilibria. At the same time the broad current profile combined with the high b_N are able to excite instabilities also in the shells fully inserted configuration.

The plasma current and safety factor time evolutions for discharges with shells fully inserted and with shells fully retracted are compared in Fig. 3.9.

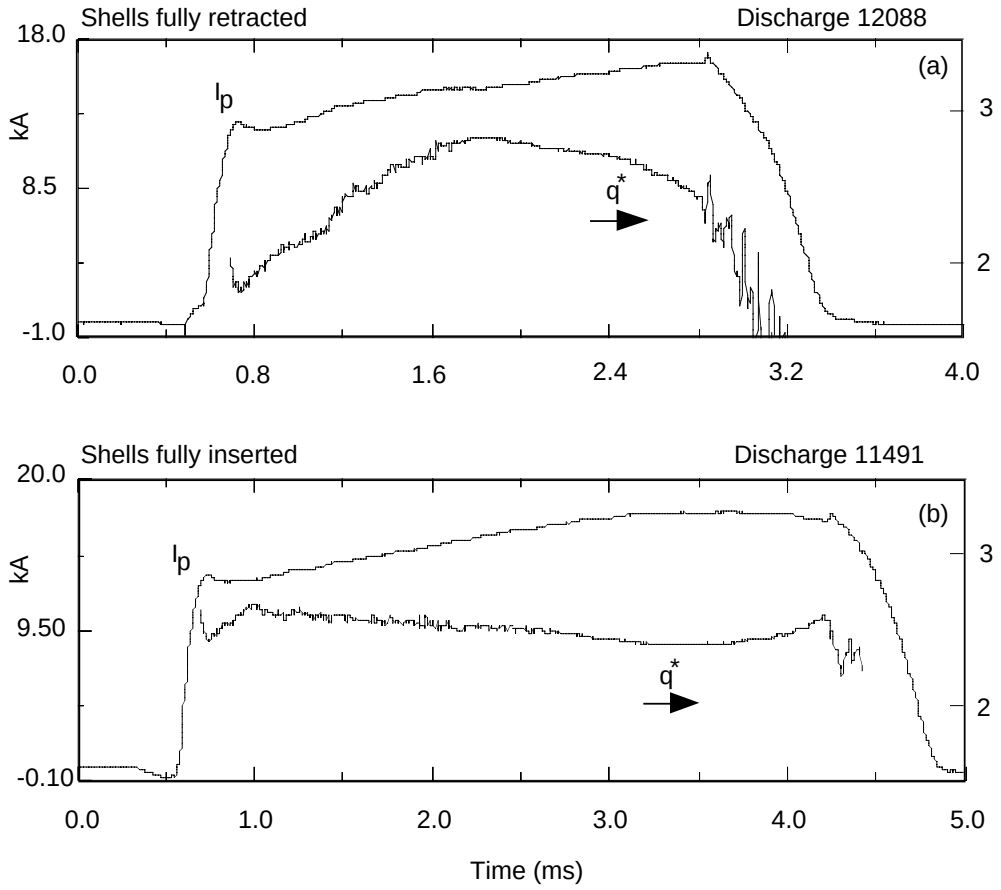

Fig. 3.9. *Time evolution of plasma current and cylindrical safety factor for discharges formed with (a) shells fully retracted and (b) shells fully inserted.*

4

Equilibrium Modeling in HBT-EP

4.1. Introduction

In order to compare the observed stability properties of the plasma discharges formed in HBT-EP as described in Chapter 3, with the predictions of ideal MHD theory, we first need to build a numerical representation of the equilibria of these discharges. As it was introduced in Chapter 2, the equilibrium reconstructions for HBT-EP plasmas are computed using the TokaMac equilibrium code. Although HBT-EP has potentially numerous diagnostics, several challenges, including a limited number of amplifier and digitizer channels, up-down asymmetry in the measurements and eddy current effects, limit the applicability of our equilibrium reconstruction procedure to a few instants in time during selected periods in some plasma discharges.

4.2 Equilibrium Reconstruction Procedure

Chapter 3 has briefly described the diagnostics used to provide measurements that can be used in the equilibrium reconstructions. In summary, the set of measurements comprises:

10 channels in the internal magnetic probe array, that measure the vertical field at the midplane in the vacuum and into the plasma edge;

30 channels in the shell mounted probe arrays, that measure the tangential field at the conducting wall;

9 channels in the array of flux loops;

4 Rogowski coils that measure equilibrium coil currents, plasma current and plasma position.

Unfortunately, because of the limited number of amplifier and digitizer channels, it is necessary to combine the data obtained from at least two identical discharges in order to use all of the above measurement points in an equilibrium reconstruction. The measurements from these multiple, nearly identical discharges are entered in a single input file for the TokaMac code which include the standard deviations derived both from systematic and shot-to-shot uncertainties as discussed below.

4.2.1 Measurement Error

Local measurements from up-down symmetric positions and measurements of the same quantity obtained from different discharges, are averaged and entered as one measurement. The standard deviation is calculated in the following manner (except for the magnetic axis):

$$\sigma_Y^2 = \left(a(\%)Y_{av}\right)^2 + \left(\frac{Y_1 - Y_2}{2}\right)^2 + Y_0^2,$$

where σ_Y is the standard deviation associated with the measurement Y, $Y_{av} = \frac{Y_1 + Y_2}{2}$, Y_1 and Y_2 are either measurements from coils in up-down symmetric positions, or from the same coil in different discharges, Y_0 is the noise level and $a(\%)$ accounts for calibration errors. The values of $a(\%)$ range from 3% for the vertical field current (2.5% is specified by the manufacturer of the Rogowski coil used for the measurement), to 20% for the shell mounted probes, for which the numerical fitting is troubled by asymmetries in the measurements from up-down symmetric positions.

The magnetic axis position, R_0, is measured by a Rogowski coil calibrated using data from an earlier internal magnetic probe [49]. In the TokaMac code, this information is

entered as a magnetic measurement of zero poloidal field at R_0. A standard deviation equivalent to 0.5 cm can be estimated from the relation:

$$B_q = \frac{rB_f}{Rq}$$

by substituting $q = 1$, $R = R_0$, and $r = 0.5$ cm.

When combining two discharges, the resulting R_0 is the average of the two measurements of the magnetic axis, $R_{0,1}$ and $R_{0,2}$, and the standard deviation is:

$$s_{B_q} = \frac{0.5B_{f,av}}{R_{0,av}} + \frac{0.5B_{f,av}}{R_{0,av}}\left|R_{0,1} - R_{0,2}\right|$$

4.2.2 Equilibrium Eddy Currents

A challenge arises in HBT-EP from the necessity of including in the reconstructions the presence of axisymmetric (n = 0) eddy currents in the shell segments, since the decay time of these eddy currents is comparable to the discharge duration. Also important are the axisymmetric eddy currents induced in the vacuum chamber segments and the *centering ring* (a two inches thick, aluminum cylinder, with two toroidal breaks, concentric to the OH coils and used to support the toroidal field magnets from the small major radius side).

The first step in addressing this problem is to approximate the conducting structures with sets of toroidally symmetric coils, as illustrated in Fig. 4.1. For simplicity we let the code treat the coils representing the centering ring as perfectly conducting (with zero net toroidal current).

For the shell and vacuum chamber segments we have decomposed the poloidal distribution of the toroidal eddy currents in orthonormal eigenmodes, as was successfully done for the vessels in the ISX-B and DIII-D tokamaks [50]. The eigenmodes implying a net toroidal current are unphysical for our toroidally segmented wall, and therefore discarded. All of the other modes correspond to having one toroidal break. Figure 4.2 illustrates, for the coils in the upper shell segment of Fig. 4.1, the first three up-down

symmetric eigenmodes with no net toroidal current, plotted versus the arc length joining the centers of the coils (with origin on the outboard midplane).

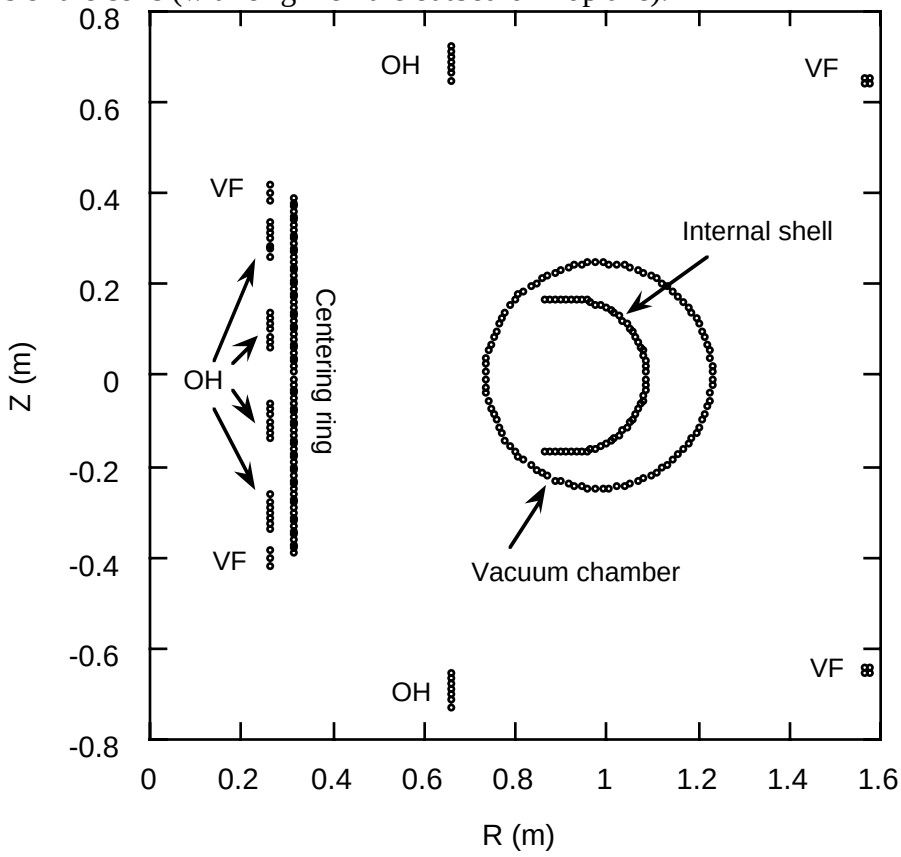

Fig. 4.1. *Coil representation of conducting structures in HBT-EP.*

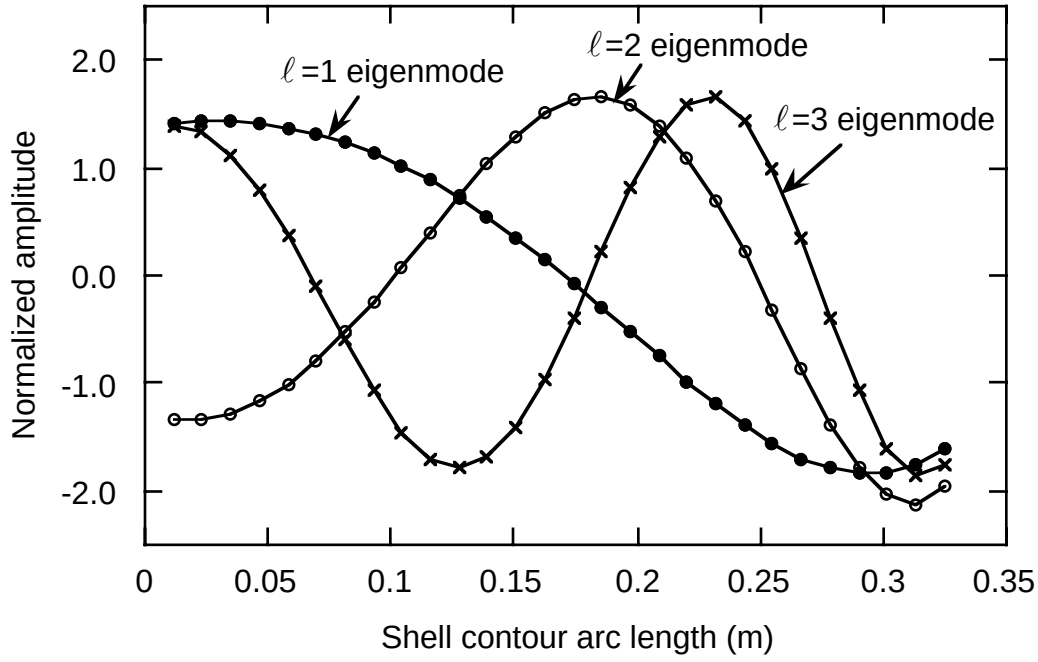

Fig. 4.2. *The first three up-down symmetric eigenmodes of the shell current.*

The eigenvalues are the R/L decay rates for the corresponding circuits. Each subsequent mode has a finer spatial scale than the next lower order mode and, therefore, a faster decay time. The calculated decay times can be corrected to include the effect of multiple toroidal breaks using the model described by Nagayama et al. for the tokamak TNT-A [51]. Table 4.1 summarizes the decay times of the ℓ = 1, 2, 3 eigenmodes for the fully inserted shells and the ℓ = 1 eigenmode for the vacuum chamber.

Eigenmode order (up-down symmetry)	*L/R* (ms) 1 toroidal break	*L/R* (ms) 10 toroidal breaks
Conducting shell		
ℓ = 1	23	12.2
ℓ = 2	13	6.9
ℓ = 3	8.4	4.5
Vacuum chamber		
ℓ = 1	1.2	0.64

Tab. 4.1. *Calculated decay times for eddy current eigenmodes in the shells and the vacuum chamber.*

The poloidal distribution of the toroidal currents in a set of coils can be prescribed in TokaMak as a linear combination of several eigenmodes. Since TokaMac is a data-analysis code, the magnitudes of each eigenmode are expected as input measurements. However, by specifying a very large standard deviation, we can effectively leave the value of the eddy currents unconstrained, and TokaMac will select the magnitudes of the equilibrium eddy currents best fitting the totality of the measurements.

We use the ℓ =1, 2, 3 eigenmodes for the eddy currents in the shells. The numerous measurements from the shell mounted probes enable the code to uniquely determine the respective magnitudes.

In the case of the vacuum chamber, the measurements are not sufficient to constrain the eddy currents without also affecting the central safety factor, q_0.

In order to select the equilibria that best represent the data, we have used the ℓ = 1 vessel eigenmode and changed systematically the current magnitude, observing the value of q_0 obtained by the fit. The result of one of these scans is shown in Fig. 4.3. It can be seen that q_0 changes following a well behaved trajectory, at least in the current range of our interest. Therefore the magnitude of the vacuum chamber eddy current can be determined from the knowledge of the safety factor at the magnetic axis of the equilibrium.

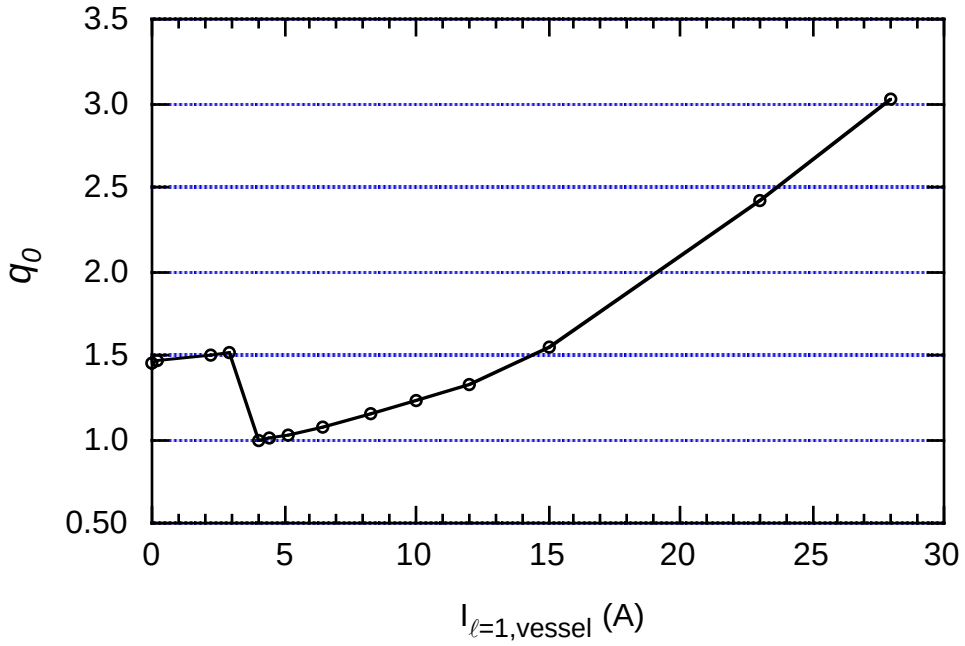

Fig. 4.3. *Relationship between the safety factor at the magnetic axis of the equilibrium and the magnitude of the $\ell = 1$ eigenmode of the vessel eddy current . Discharges 11491, 12187, 12200 (shells fully inserted).*

A proper description for the evolution of the q profile during sawtooth oscillations in tokamak plasmas has yet to be formulated [52]. Observations in JET [53] suggest that the value of q on axis stays close to unity from below during the entire sawtooth cycle. However, since the stability codes usually fail in determining the boundary to external modes for equilibria having $q_0 < 1$, in this thesis we have generated discharges with clear sawtoothing oscillation and assumed $1.02 < q_0 < 1.04$ during the sawtoothing periods, i.e. we have assumed the lowest possible value of q_0 before incurring in unphysical results from the stability analysis.

To test our procedure for determining the eddy currents, we look at the time development of the $\ell = 1$ shell and chamber eigencurrents for two sawtoothing discharges, in the wall fully retracted (Fig. 4.4) and wall fully inserted (Fig. 4.5) configurations.

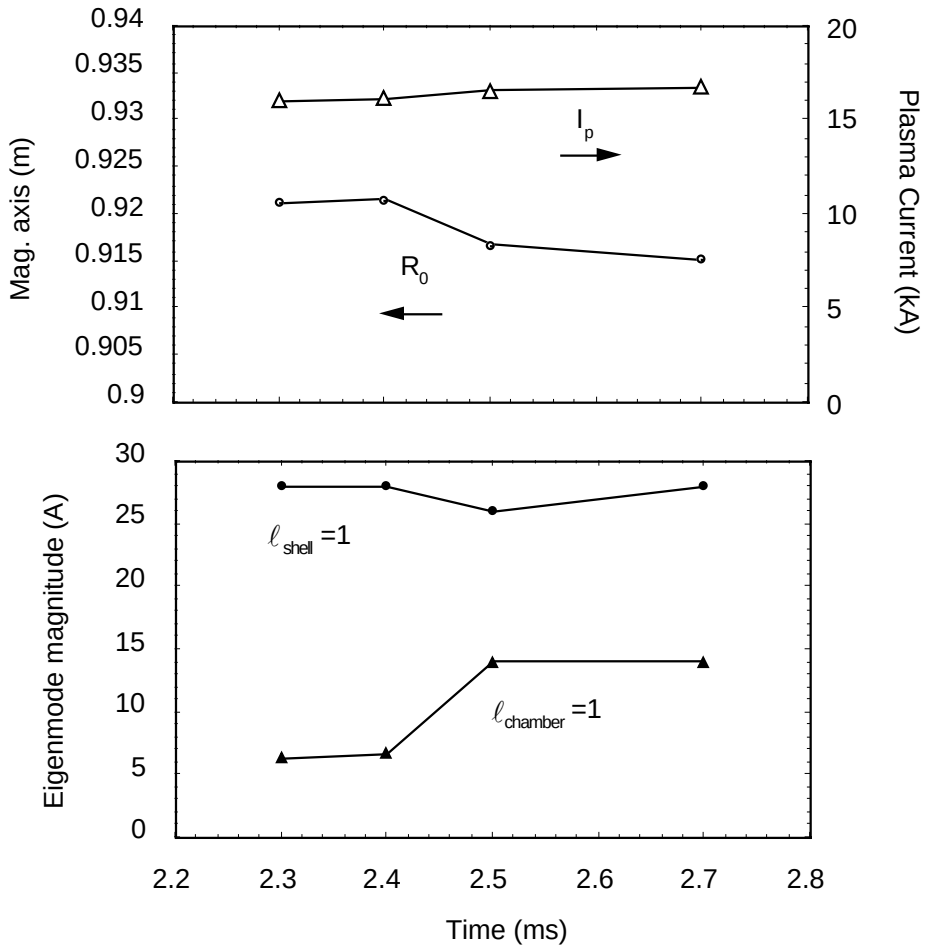

Fig. 4.4. *Time evolution of the $\ell = 1$ shell and vessel current distributions calculated through equilibrium reconstructions of discharges formed with the conducting shells fully retracted. The evolution of the plasma current and magnetic axis position are shown for comparison. Discharges 12088, 12094.*

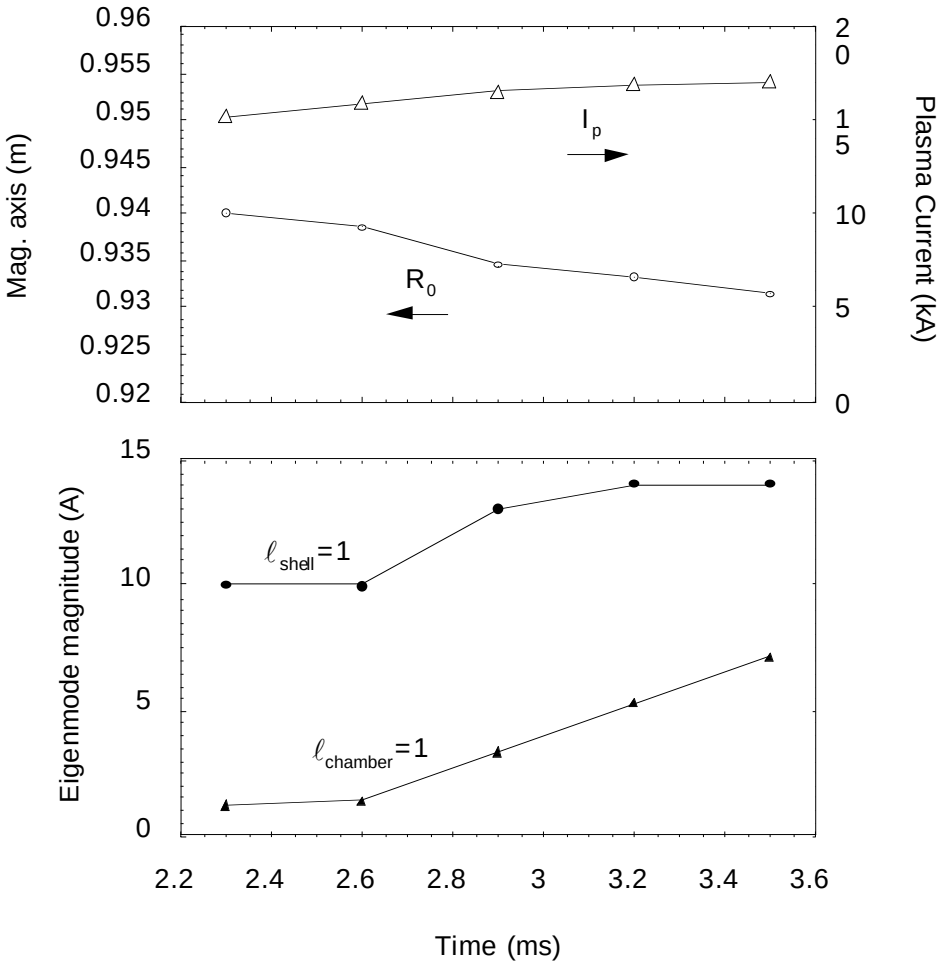

Fig. 4.5. *Time evolution of the calculated $\ell = 1$ shell and vessel current distributions, plasma current and magnetic axis position for discharges formed with the conducting shells fully inserted. Discharges 11491, 12187, 12200.*

It is evident that memory of the initial field start-up is present only in the shell eigencurrents, consistently with the calculated decay times. Both the slightly positive current ramp and the changes in the plasma position contribute to drive eddy currents in shell and vacuum chamber, the latter showing a faster response.

Notice that when the shells are fully extracted the magnitudes of the $\ell = 1$ shell and chamber eigenmodes are about twice as large as when the shells are fully inserted.

This can be expected because, as described in Chapter 3, the shell segments are designed to conform to the plasma in the shells-fully-inserted configuration. When the

shells are fully retracted the shell segments do not conform as well to the flux surfaces calculated in absence of an internal wall, therefore larger shell eddy currents are induced by the larger field line bending that is required. This intuition is confirmed by calculations of the eddy currents carried out using a filament code in which the shells are represented by perfectly conducting coils. Figure 4.6 shows results of these calculations for the shells fully retracted and the shells fully inserted configurations with same plasma and equilibrium coils currents. The current values listed in the figure are those of the current in the shell coils and are consistently larger for the simulation with shells fully retracted.

Moreover, when the shells are fully retracted, the shell segments do not conform as well, and are closer, to the vacuum chamber. Therefore the chamber eddy currents should also be expected to be larger than in the shells fully-inserted configuration.

Figures 4.7 and 4.8 show flux surfaces and representative profiles from the equilibrium reconstruction at t = 3.2 ms for the discharges of Figs. 4.3 and 4.5. Using the reconstructed pressure distribution we have simulated the signal of our soft x-ray detector array, assuming a constant density across the plasma and bremsstrahlung as emission mechanism. In the comparison with the actual measurements illustrated in Fig. 4.7(c), the amplitude of the simulated signal has been arbitrarily scaled and the spread is due to uncertainties in the geometry of the diagnostic. The comparison shows good agreement between the measured and reconstructed profiles.

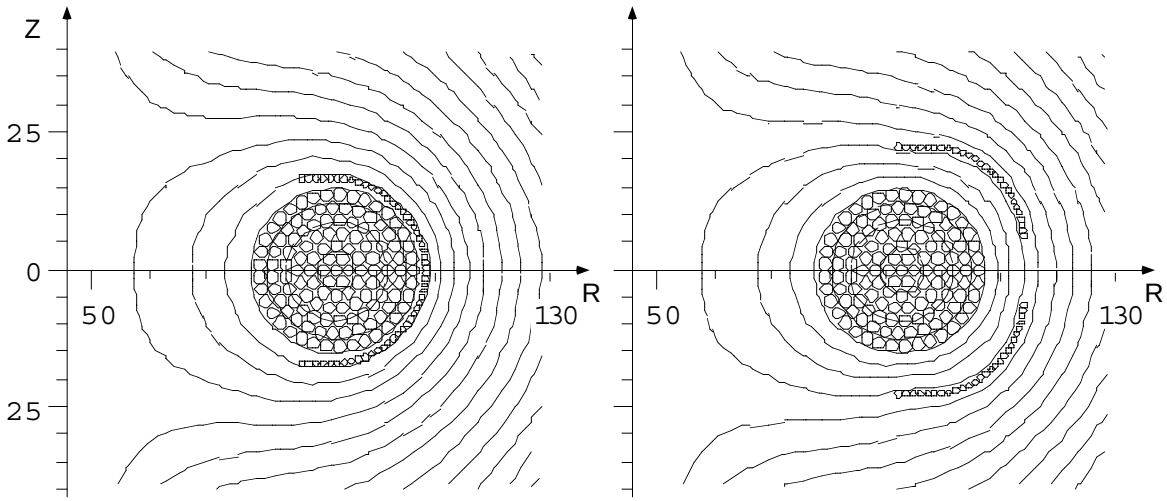

R (cm)	Z (cm)	CURRENT (A)
86.24	16.64	-310.3603
87.56	16.64	-0.6303
88.83	16.64	-5.1962
90.10	16.64	24.2639
91.37	16.64	19.8859
92.62	16.61	7.6614
93.87	16.52	-9.1010
95.11	16.35	-21.8880
96.32	16.06	-40.8747
97.51	15.63	-12.4556
98.67	15.11	-6.7047
99.75	14.54	-38.4636
100.80	13.77	17.3941
101.68	13.02	81.2317
102.59	12.29	35.1492
103.44	11.50	40.4670
104.23	10.66	34.7836
104.97	9.77	49.6077
105.67	8.82	8.0650
106.25	7.84	45.8063
106.79	6.81	26.5735
107.26	5.75	34.2179
107.66	4.71	15.8412
107.98	3.64	14.7820
108.23	2.60	-10.1876
108.36	1.56	23.6565
108.48	0.51	-23.4866

R (cm)	Z (cm)	CURRENT (A)
91.90	22.30	393.0181
93.22	22.30	98.5451
94.49	22.30	113.8630
95.76	22.30	85.1862
97.03	22.30	52.6729
98.28	22.27	19.5786
99.53	22.18	-8.0800
100.77	22.01	-32.5876
101.98	21.72	-56.4710
103.17	21.29	-47.2717
104.33	20.77	-52.8451
105.41	20.20	-83.8142
106.46	19.43	-57.6975
107.34	18.68	-11.9881
108.25	17.95	-51.4902
109.10	17.16	-50.7998
109.89	16.32	-54.6056
110.63	15.43	-47.5944
111.33	14.48	-67.8607
111.92	13.50	-42.5226
112.46	12.47	-48.6764
112.92	11.41	-36.5985
113.32	10.37	-37.2814
113.64	9.30	-25.8960
113.89	8.26	-27.7126
114.02	7.22	3.5326
114.14	6.17	75.4073

Fig. 4.6. *Shell coil currents calculated using a filament code in shells fully retracted and shells fully inserted configurations with same plasma, OH and VF coil currents.*

Fig. 4.7. *Measured profiles and equilibrium reconstruction for discharges 11491, 12187, 12200 at t = 3.2 ms: (a) poloidal flux surfaces with magnetic measurement locations, soft x-ray viewing chords and coil representation of conducting structures; (b) measured and fitted profiles of vertical field at IMP locations; (c) measured and simulated profiles of chord-integrated SXR emission; (d) safety factor, current density and pressure from equilibrium reconstruction.*

Figure 4.7(b) shows the measured and fitted profiles of the poloidal field measured by the internal magnetic probe array. Analogously, in Fig. 4.8 are shown the input profile (average of measurements from up-down symmetric positions) and the fitted profile of the poloidal field measured by the shell mounted probes. The convention for the shell arc length used in the plotting has been described in Fig. 3.3.

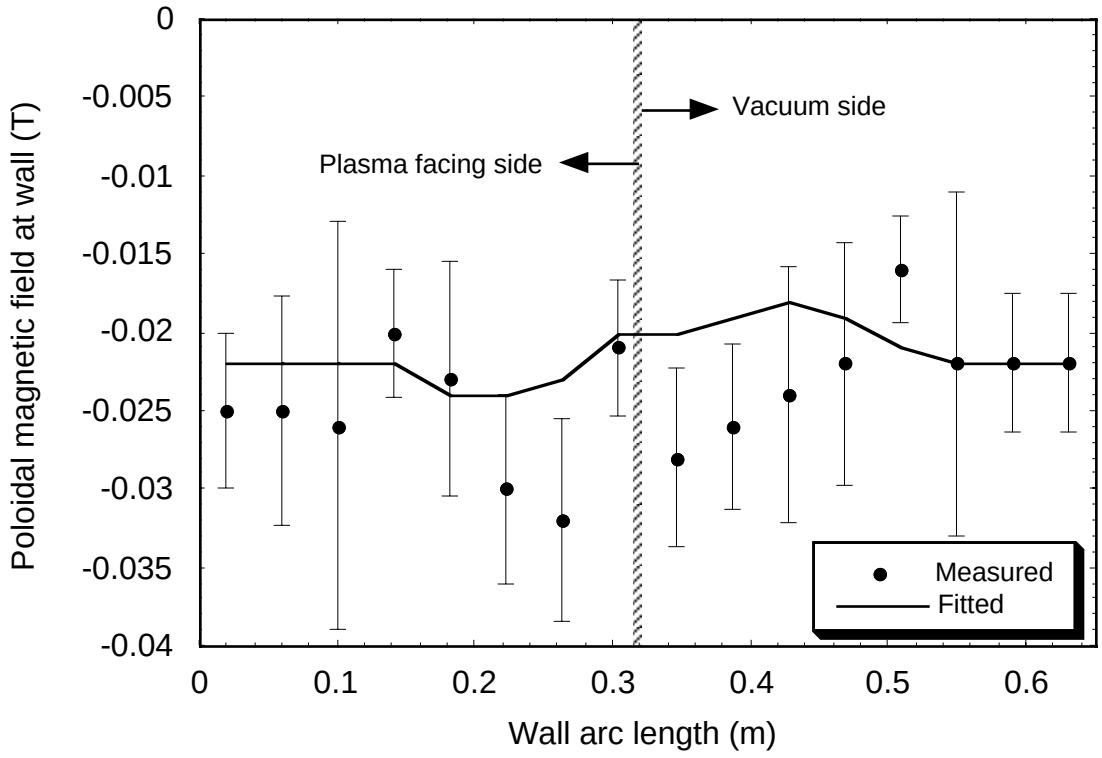

Fig. 4.8. *Input and fitted profiles of poloidal field at the locations of the magnetic probes mounted on the upper shell segment for the discharges of Fig. 4.7. The shell arc length is intended as described in Fig. 3.3.*

The calculated global parameters show little variations with the order of the polynomials used to parametrize the functions $p(\psi)$ and $F(\psi)$, if the order of the pressure polynomial is greater than one, as illustrated in Figs. 4.9(a) and 4.9(b). A choice of third order polynomial for $p(\psi)$ and fifth order polynomial for $F(\psi)$ is assumed in all of the equilibrium reconstructions reported in this thesis, unless specified differently. This combination gives the highest order of polynomials that can be used before incurring in unphysical oscillations in the fitted profiles. Figure 4.9 shows that the use of a third order polynomial for $p(\psi)$ (two terms in the polynomial representation of $p\psi$) leads to the highest values of β_N and to values of q_{edge} that are the closest to $q = 3$ from below. From a comparison with the boundary thresholds for external kink plotted in Fig. 2.4, one can see

that this corresponds to the most unstable equilibria. As will be shown in the next chapter, the stability predictions carried out on equilibria calculated with this choice of polynomial orders are consistent with the experimental results obtained in different plasma-wall configurations.

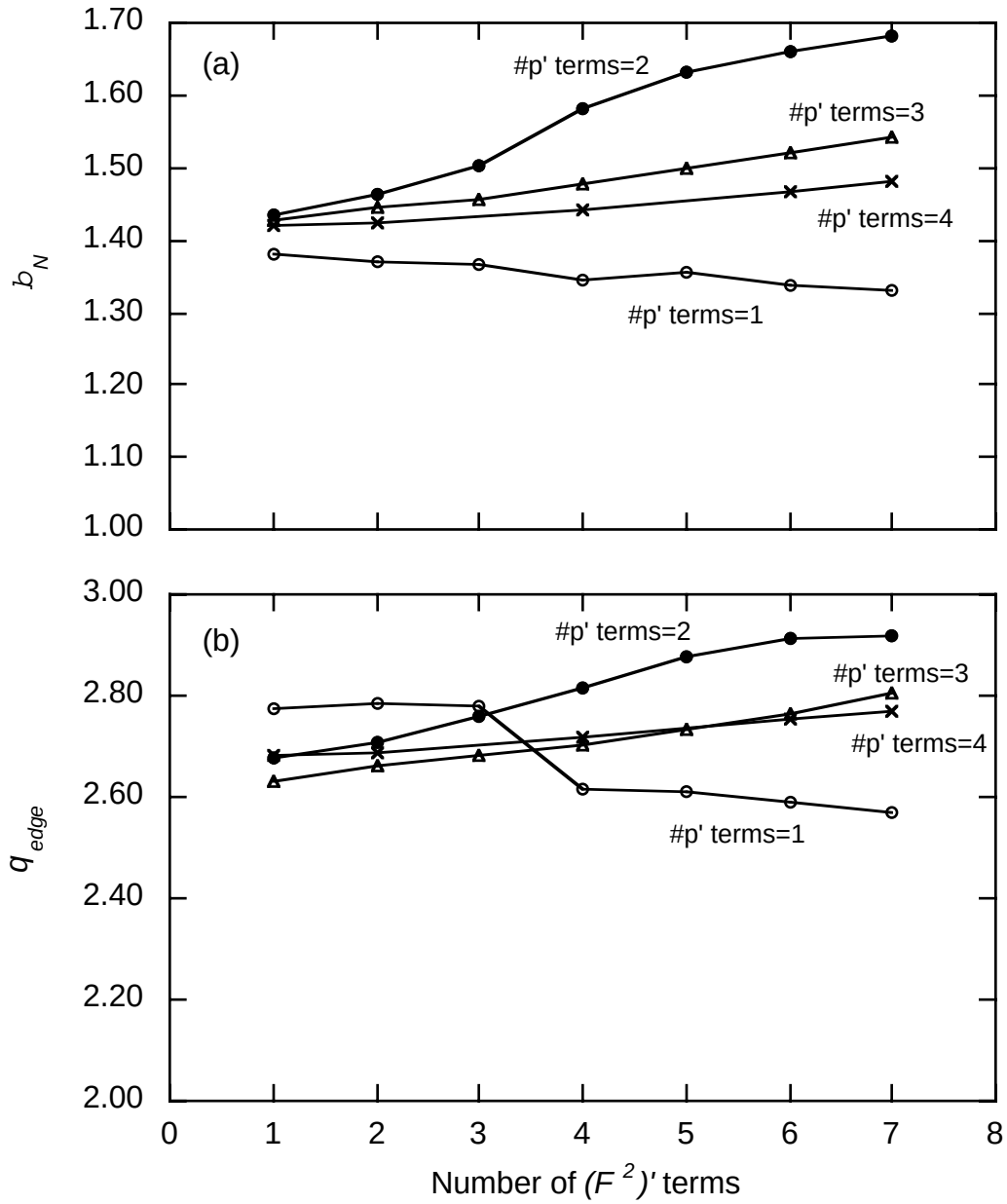

Fig. 4.9. *Dependence of (a)* b_N *and (b)* q_{edge} *on the order of the polynomials modeling* $p(y)$ *and* $F(y)$*, for the discharges of Figs. 4.7 and 4.8.*

5

Experimental Results and Comparisons with Ideal MHD Theory

5.1. Introduction

It was stated in Chapter 1 that the goal of this thesis is to improve our understanding of the interaction of a segmented, resistive wall with external kink instabilities. In order to achieve this goal this chapter will address the following open questions.

As it was said in Chapter 2, for the stability calculations we model HBT-EP's segmented wall with a continuous, perfectly conducting wall. Does the segmentation prevent the helical patterns predicted for the continuous wall, to close on the actual wall?

In Chapter 3 we said that for high frequency magnetic fluctuations the resistive wall should effectively behave like a perfectly conducting wall. Is this true?

And finally, what is the global effect of the wall on stability?

The same equilibrium reconstruction procedure has been applied to same minor radius plasmas formed with wall fully retracted and with wall fully inserted. The reconstructions are performed for time points at which different discharges reach the same regions of parameter space, but from which the plasmas develop in different ways.

5.2. Stability Boundaries

For discharges with wall fully retracted, rapidly growing precursors (growth time $\gamma^{-1} \leq 200$ ms), that appear rotating with frequency $f_{mode} \approx 8$ kHz, result in current disruptions when the edge safety factor decreases below 3 and β_N reaches values close to 1.5 (Fig.

5.1). With the wall fully inserted (Fig. 5.2) similar instabilities are consistently observed to grow at a slower rate ($\gamma^{-1} \approx 600$ ms).

The values of β_N and edge safety factor, q_{edge}, from equilibrium reconstructions are symbolized in Figs. 5.1 and 5.2 by solid circles. These values are in good agreement with the time evolutions of the same quantities estimated from toroidal force balance using magnetic measurements of the poloidal beta [53, 27], and shown in the same figures as solid traces. The PEST-VACUUM stability analysis, conducted in the absence of any wall, places the discharge of Fig. 5.1 (12088, 12094) near the stability boundary against external kinks [gray shaded area in Fig. 5.1(a)], calculated at the time when the growth starts to occur ($\gamma_{PEST}^{-1} \gg 90$ ms). The discharge of Fig. 5.2 (11491, 12187, 12200) is predicted 10% above marginal stability at t = 3.2 ms, with growth $\gamma_{PEST}^{-1} \gg 30$ ms.

In the case with wall fully retracted, adding the model wall does not significantly change the predicted stability boundary [cross-hatched area in Fig. 5.1(a)]. In the case with wall fully inserted however, the model wall stabilizes the plasma and doubles the critical β_N [Fig. 5.2(a)].

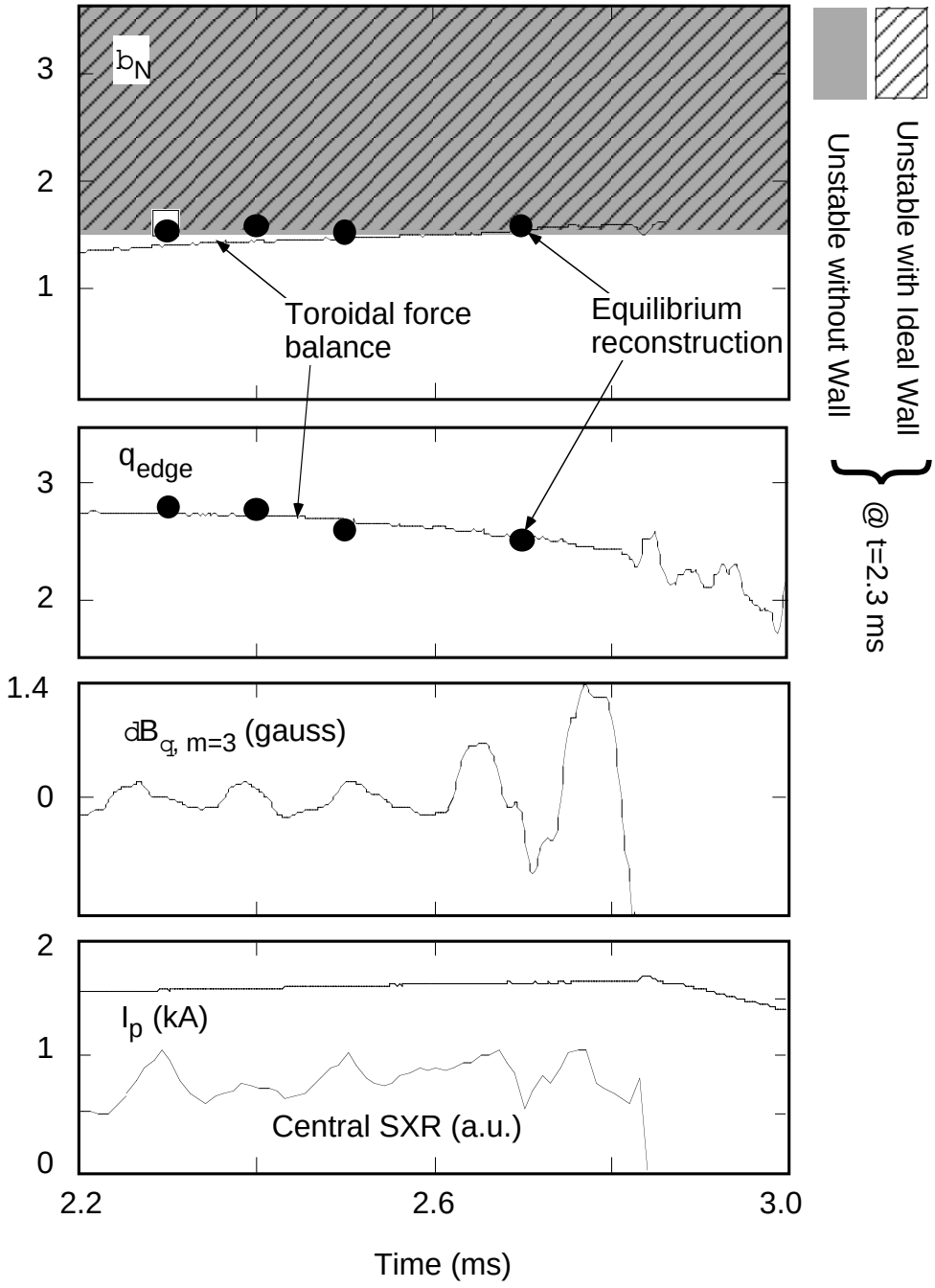

Fig. 5.1. *Disruptions induced by MHD instabilities in discharges with wall fully retracted. Solid circles represent values from equilibrium reconstructions, hollow symbol is for companion flux conserved equilibrium with increased beta. Cross-hatched and shaded areas show the predicted stability boundaries calculated respectively with and without an ideal wall at t = 2.3 ms.*
(a) Normalized beta, (b) edge safety factor, (c) m/n = 3/1 magnetic fluctuations (d) plasma current and central chord of the soft x-ray diagnostic. Discharge 12088.

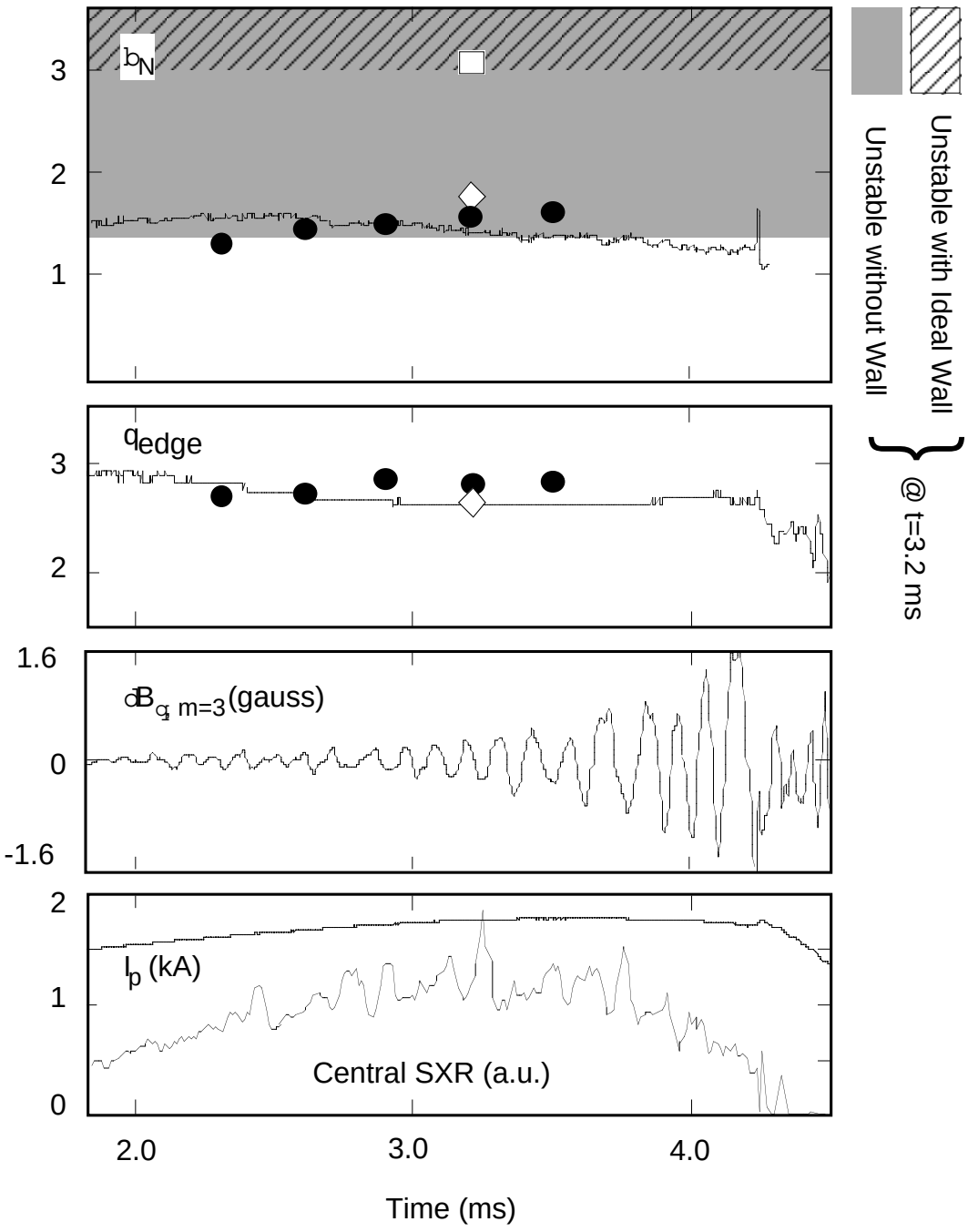

Fig. 5.2. *Slowly growing precursors in discharges with wall fully inserted. Hollow symbols represent companion equilibria with increased beta (□) and with decreased shear (◇). Predicted stability boundaries are calculated at t = 3.2 ms. Discharge 11491.*

5.3. Mode Structure

In both discharge cases, toroidally distributed Fourier-analyzing Rogowski coils and Mirnov loops identify the instability as a global $n = 1$ kink mode, with a large $m = 3$ component calculated to have a resonant q surface in the vacuum. Figures 5.3(a, b, c) show for the discharge of Fig. 5.1, our observations of the various poloidal components. The $m = 2$ and $m = 3$ fluctuations in the poloidal magnetic field are detected at the same minor radius by Fourier analyzing Rogowski coils. The odd m components of the plasma radial displacement in Fig. 7(a), are estimated from the fluctuating part of the chord-integrated soft x-ray intensity profile as described in Chapter 3. Given our viewing solid angle, the displacement spans only the plasma core. The fluctuation localized near the magnetic axis, where we assume that $q \gg 1$, is identified as a mode number $m = 1$.

The similar fluctuation frequency for the measured components, together with observations in some cases of $n = 2$, $m = 3$ fluctuations having a double frequency, suggest rigid toroidal rotation of these plasmas.

The predicted mode structure, shown in Fig. 5.3(d), is consistent with the experimental mode identification.

Analogously in Fig. 5.4 is illustrated the comparison of measured and calculated mode structure for the discharge of Fig. 5.2.

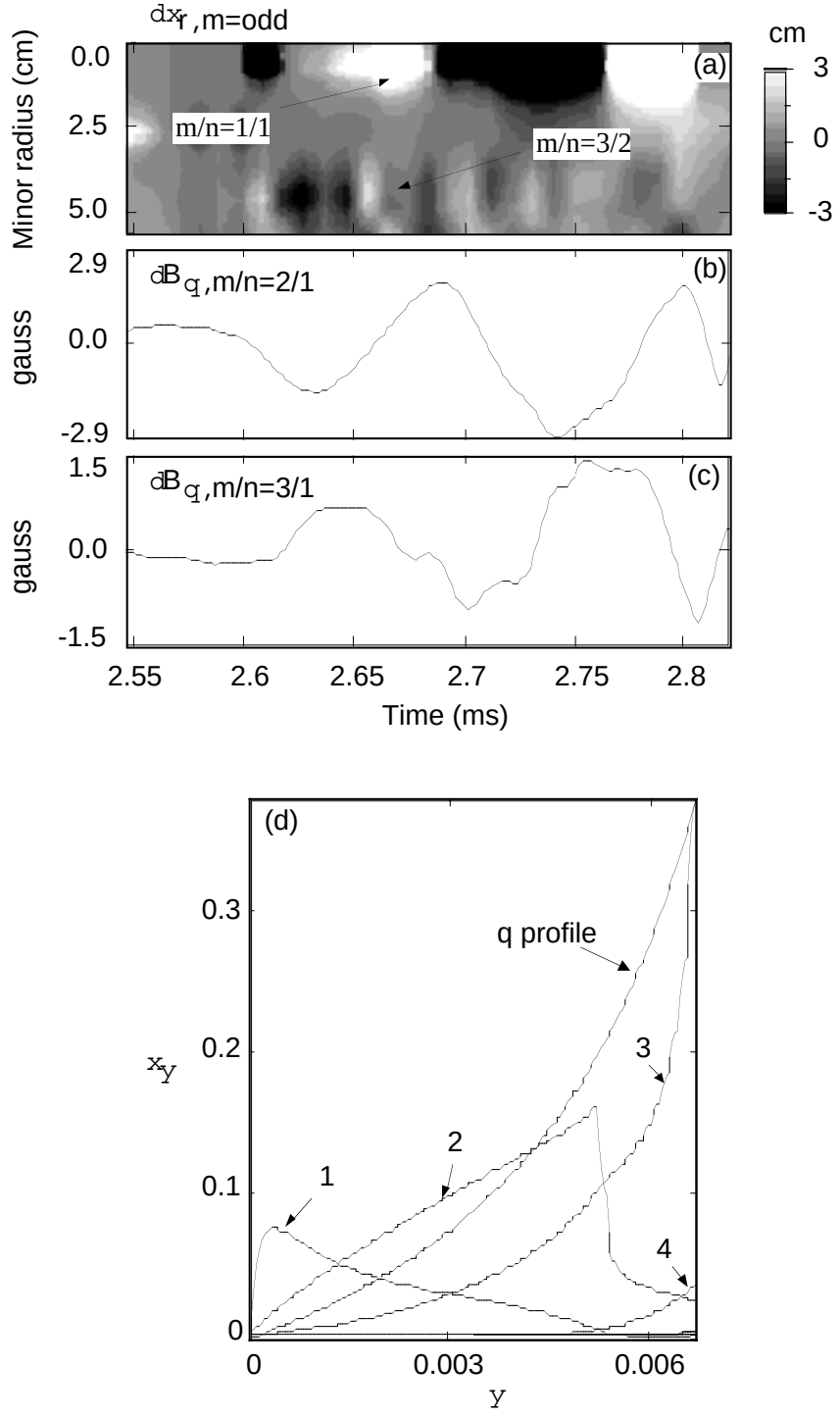

Fig. 5.3. *Comparison of measured and calculated mode structure for discharge 12088. (a) Radial plasma displacement for odd m components in the core region; (b) m = 2 and (c) m = 3 Fourier analyzing Rogowski coil signals; (d) radial dependence of different Fourier components of the normal plasma displacement for the instability calculated by pest without an ideal wall.*

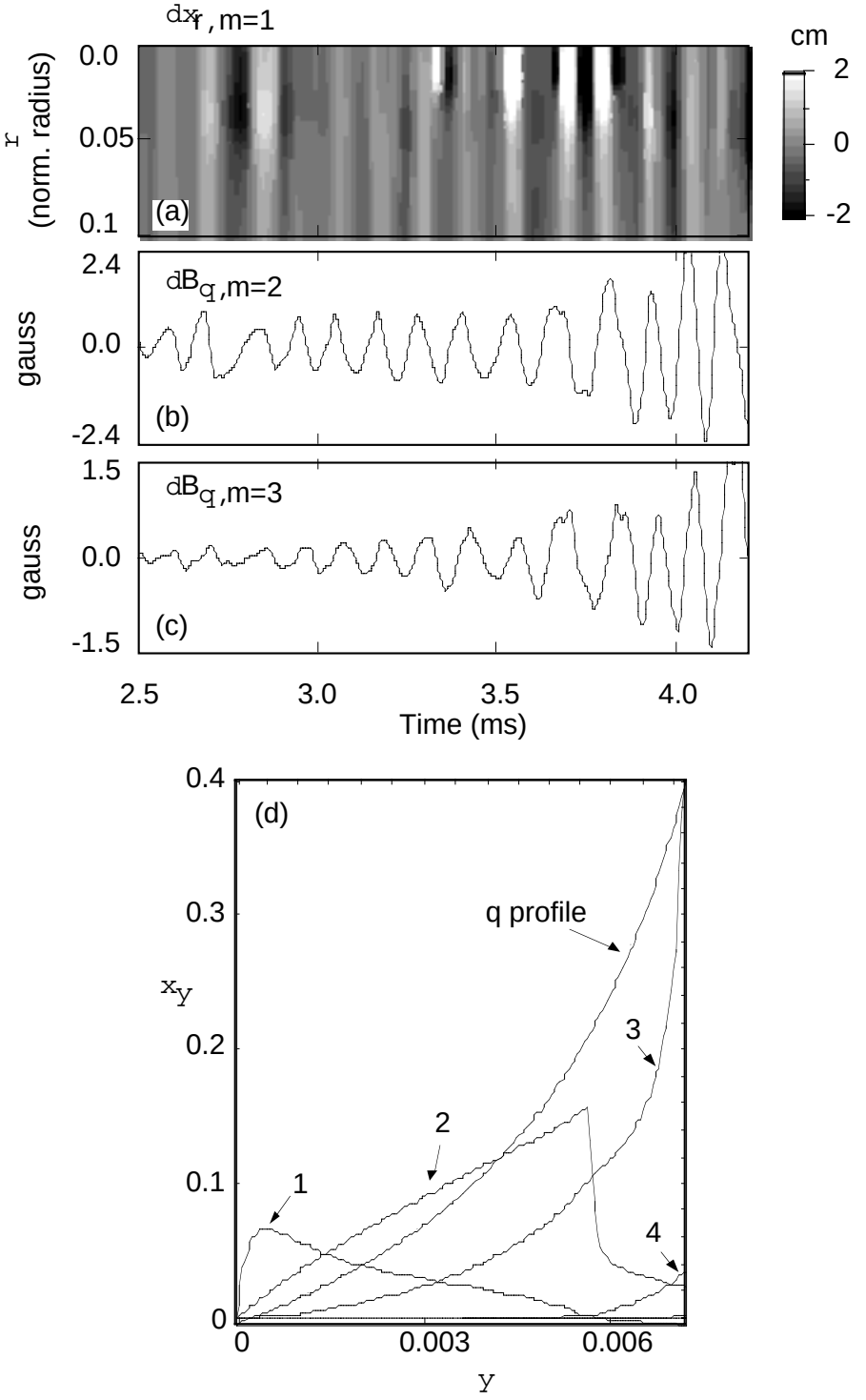

Fig. 5.4. *Comparison of measured and calculated mode structure for discharge 11491. (a) Radial plasma displacement for odd m components in the core region; (b) m = 2 and (c) m = 3 Fourier analyzing Rogowski coil signals; (d) radial dependence of different Fourier components of the normal plasma displacement for the instability calculated by pest without an ideal wall.*

5.4. Eddy Currents

Figure 5.5(b) shows the toroidal component of the instability-induced eddy currents measured on the plasma facing side of the wall for the wall retracted discharge of Fig. 5.1, before and during the disruption. The image is obtained linearly by interpolating among the 15 measurements distributed on the plasma facing side of the two instrumented wall segments of Fig. 3.3. Given the rigid toroidal rotation of the plasma, we compare the eddy currents that PEST-VACUUM calculate over one period in the toroidal angle [Fig. 5.5(c)] with the measurements taken over a time interval $\tau = 1/f_{mode}$ [Fig. 5.5(d)]. When the codes find stability in presence of the ideal wall, to obtain the eddy current pattern for the comparison we have either scaled up the pressure in flux conserved equilibria [40], or recalculated the equilibrium with increased q on axis. These "companion" equilibria are represented by hollow symbols in Figs. 5.1 and 5.2. In the wall retracted case the 3% increase in β_N for the companion equilibrium is within the uncertainties of the calculations for the original reconstruction. The exact matching of the pitch of the current patterns, is a further confirmation of our mode identification.

To carry out the comparison in more detail, we have picked a phase of the poloidal distribution of the toroidal eddy current [phase I in Fig. 5.5(d)] and compared the code calculations with the average of measured distributions having the same phase at different time points. The amplitude of the measured eddy current have been arbitrarily scaled for comparison with the theoretical profiles.

Figure 5.6(a) shows good general agreement for wall retracted, with deviations toward the outboard gap (*shell arc length* = 0), where the bulge in the model wall allows the eddy currents to smoothly go to zero at the mid-plane. Figure 5.6(b) shows the analogous comparison for the wall inserted discharge 11491, with good general agreement except toward the edges by the inboard gap, for reasons that will be discussed later.

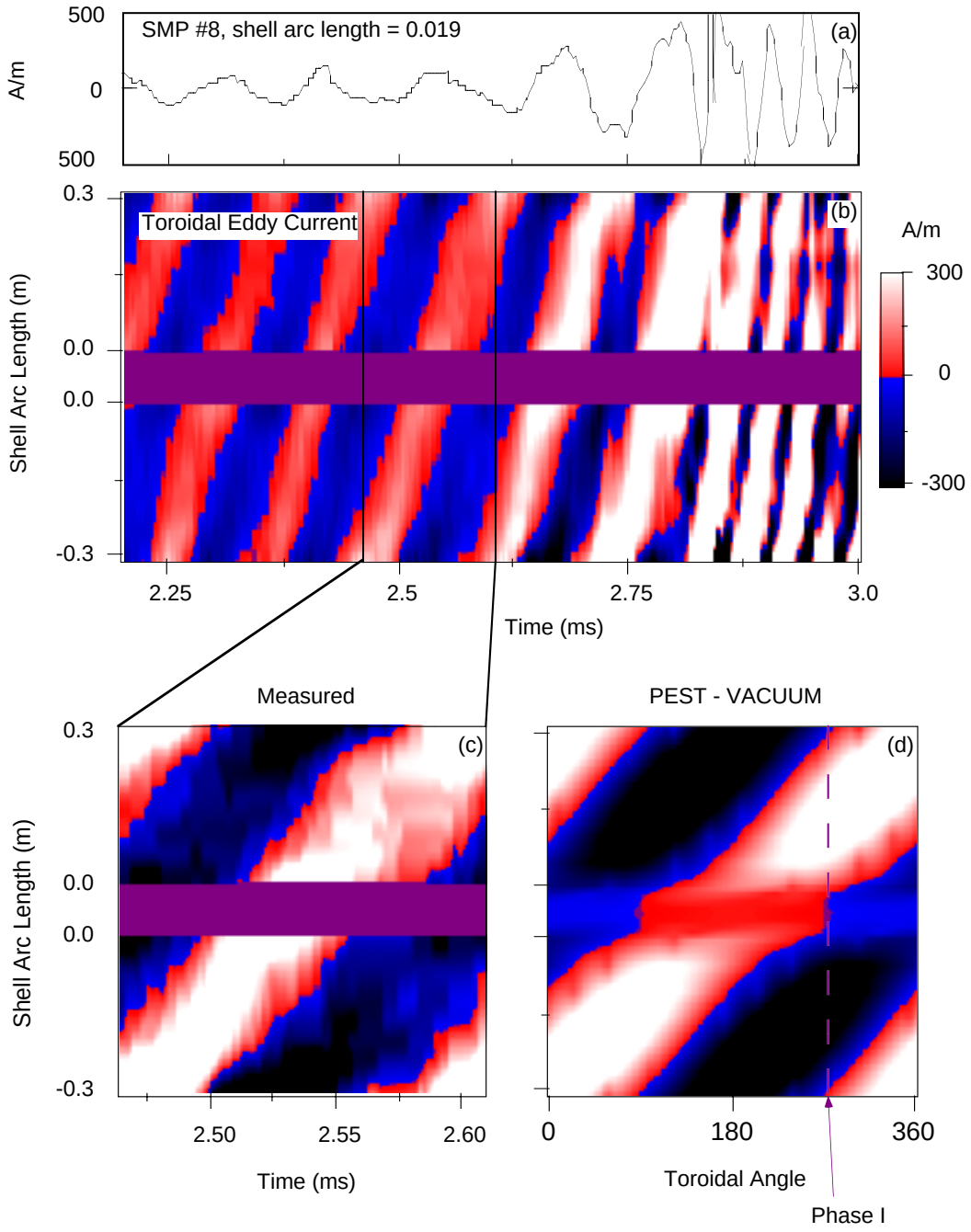

Fig. 5.5. *Toroidal component of the instability-induced eddy currents on the plasma-facing side of two wall segments during discharges with wall fully retracted. (a, b, c) Time evolution; (d) pattern calculated by PEST1-VACUUM. Discharge 12088*

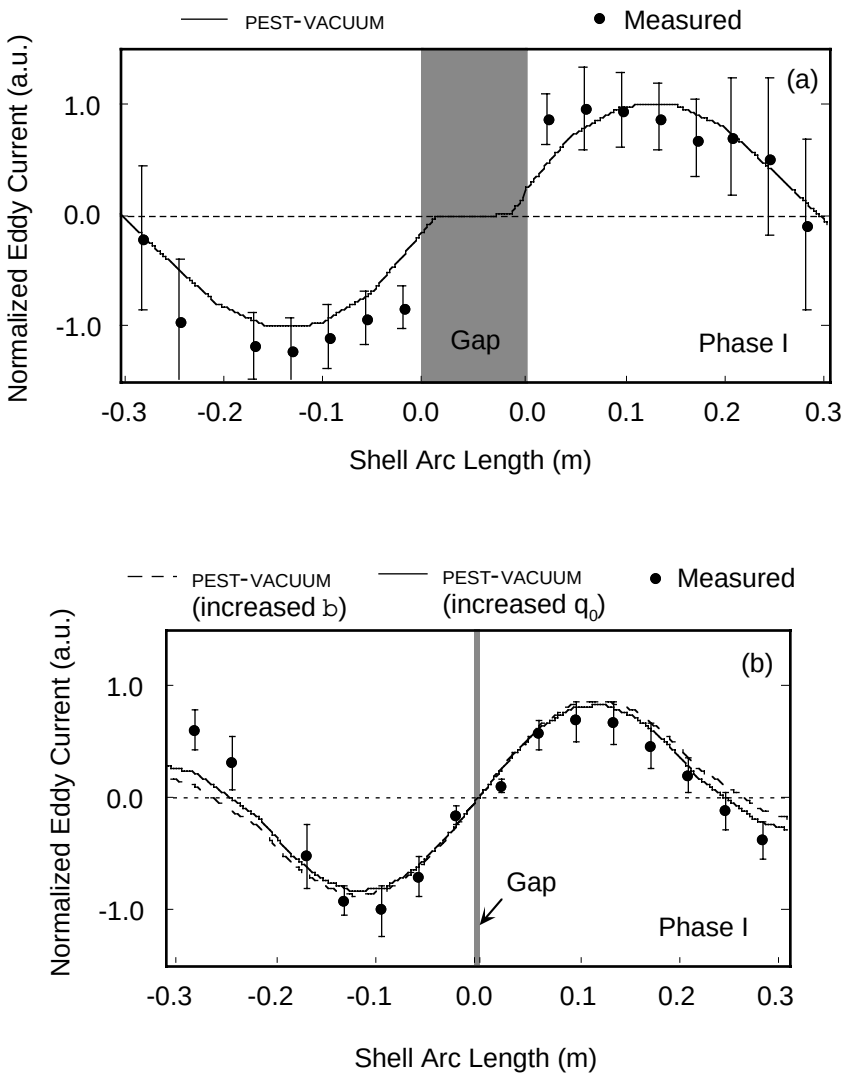

Fig. 5.6. *Comparison of measured and predicted eddy currents showing the poloidal distribution at phase I of Fig. 5.4(d) for (a) wall fully retracted, discharge 12088, and (b) wall fully inserted, discharge 11491.*

Figure 5.7 shows for a wall-inserted discharge similar to 11491, the eddy currents measured by all 16 probes in the top wall segment (Fig. 3.3). The measured change in pattern from the plasma-facing to the vacuum side of the wall corresponds to the predictions for the ideal wall, confirming our initial assumptions that the instability-induced eddy currents do not leak through the wall.

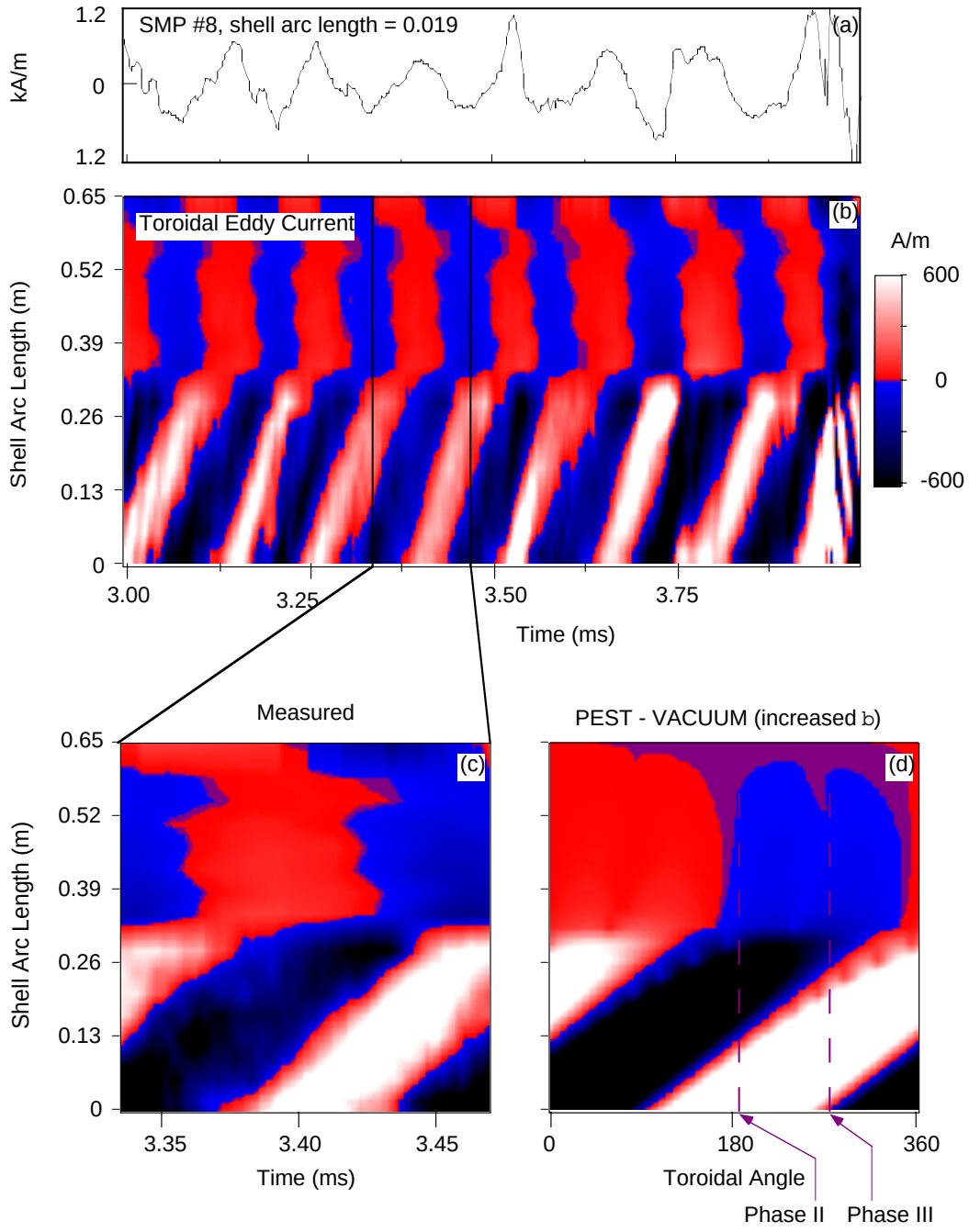

Fig. 5.7. *Toroidal component of the instability-induced eddy currents on the plasma-facing and vacuum side of one wall segment during discharges with wall fully inserted. (a, b, c) Time evolution; (d) pattern calculated by PEST1-VACUUM. Discharge 12200.*

In Figs. 5.8 and 5.9 the detailed comparisons of measurements and predictions are carried out for both wall inserted and wall retracted cases at two phases. At phase II the predicted poloidal distribution on the plasma facing side of one wall segment sums to zero. At phase III (90˚ apart), the predicted distribution is mostly unipolar. Again the agreement is generally good, with most significant differences appearing in phase III.

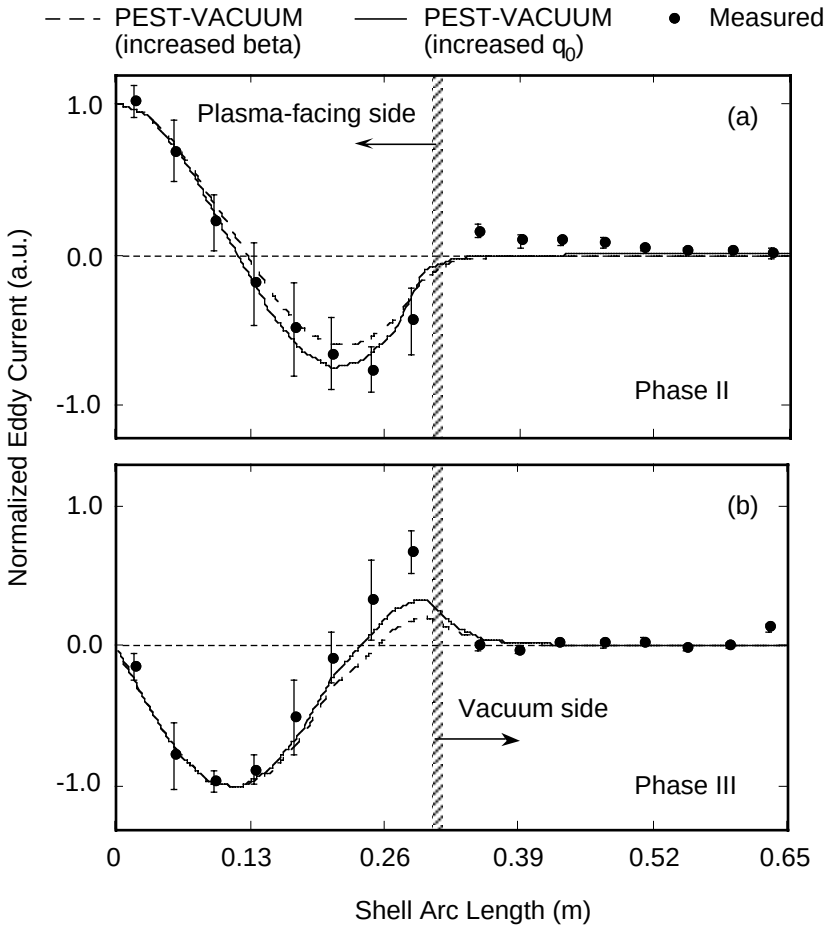

Fig. 5.8. *Comparison of measured and predicted eddy currents showing the poloidal distribution at (a) phases II and (b) phase III of Fig. 5.7(d) for the wall fully inserted discharge 12200.*

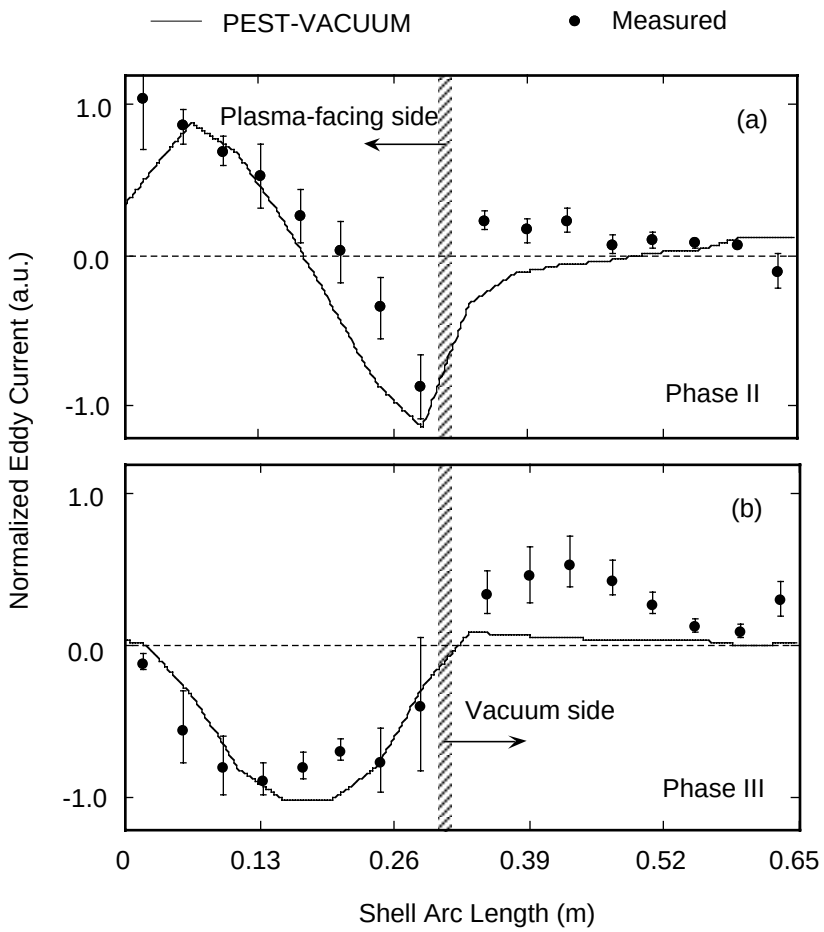

Fig. 5.9. *Comparison of measured and predicted eddy currents showing the poloidal distribution at (a) phases II and (b) phase III of Fig. 5.7(d) for the wall fully retracted discharge 12094.*

To understand these deviations we first need to note that in the code calculations, the poloidal distribution of the toroidal eddy current always sums to zero on the plasma facing side of the wall (Fig. 5.6), and stays close to zero on the vacuum side (Figs. 5.8, 5.9). The presence of a gap where the code has a bulge implies that when a mostly unipolar current distribution is predicted to occupy the entire plasma-facing side of one wall segment [as in Figs. 5.6, 5.8(b), 5.9(b)], deviations must appear in the measured pattern to allow for the return currents. From the measurements we see that these return currents tend to flow mostly:

- near the edges of the segment in the wall fully inserted configuration [Fig. 5.8(b) at *shell arc length* = 0.3 and 0.65]

- on the vacuum side of the wall in wall fully retracted configuration [Fig. 5.9(b) for *shell arc length* > 0.3].

In the latter case it is possible that these return currents decrease the (small) stabilizing radial field predicted by the code in correspondence of the outer mid-plane gap.

5.5. Summary of Comparison Results

Experimental measurements of $n = 1$, rotating instabilities in HBT-EP have been compared to the predictions of ideal MHD numerical codes. The instabilities rotate with respect to the laboratory frame at 7% of the Alfven frequency, $w_A = V_A/qR$.

Table 5.1 summarizes, in terms b_N, the results of the stability calculations for the two plasma-wall configurations investigated.

	Critical b_N with ideal wall at infinity, $b_{N,\infty}$	b_N of the equilibrium	Critical b_N with ideal wall at actual b/a, $b_{N,b}$
$\langle b \rangle/a$ = 1.52 t = 2.3 ms	1.51	1.56	1.57
b/a = 1.07 t = 3.2 ms	1.4	1.58	3.0

Table 5.1. *Values of b_N and critical b_N for the equilibria of Figs. 5.1 and 5.2.*

With the resistive wall at $\langle b \rangle/a = 1.52$ the predicted marginal stability boundaries in the presence of the ideal wall and with the ideal wall at infinity are almost coincident. The numerical procedure predicts accurately the destabilization of fast-growing, global, external modes.

When the wall is inserted at b/a = 1.07, the fast growing instabilities predicted without a conducting wall are stabilized, consistently with the elevated critical β_N calculated in presence of the ideal wall. The nature of the residual instabilities that are observed has not been undestood, yet. The stability boundary predicted in absence of the wall seems to be of significance in this case. The mode structure of these instabilities is consistent with the calculations for ideal, external modes, although the growth rates are much slower and close to the resistive time scale of either the wall or the plasma.

The measurements of the eddy current patterns induced on both plasma-facing and vacuum sides of HBT-EP's thick, segmented wall, are a useful tool for mode identification. The excellent agreement with the patterns predicted on the model wall demonstrate that for high frequency fluctuations the wall behaves as ideal, and that the segmentation does not prevent, at least away from the edges, the eddy current from approximating the helical patterns predicted for a continuous wall. These eddy current can account for the stabilizing effects observed when the wall is fully inserted.

6

Conclusions

6.1 Discussion of the Results

Plasma discharges near the marginal stability boundary to $n = 1$ external kink modes have been formed in HBT-EP with the same minor radius but different wall configurations: wall fully retracted and wall fully inserted. The plasma formation technique combines a rapid formation start-up with a slow current ramp-up to create high b_N plasmas with a broad current profile and clear sawtooth oscillations that indicate values close to unity for the safety factor at the magnetic axis.

The equilibria have been carefully reconstructed, using the numerous available external and internal magnetic measurements, an eigenmode representation of the equilibrium eddy currents induced in the segmented wall and vacuum chamber, and the assumption $1.02 < q_0 < 1.04$ during sawtooth cycles.

The accuracy of the procedure is supported by the results of several tests. Good agreement has been shown between measured soft x-ray profiles and simulated profiles obtained using the reconstructed pressure distributions. Time evolutions and magnitudes of the equilibrium eddy currents in wall and vacuum chamber are consistent with expectations and calculations performed with a filament code. The values of b_N and q_{edge} calculated in the equilibrium reconstructions are in good agreement with the same quantities estimated from toroidal force balance. When instabilities develops, the observations of stability thresholds and mode structures are consistent with the predictions of ideal MHD theory. The patterns of the instability-induced eddy currents measured on the wall for the two

different wall positions are in excellent agreement with the patterns calculated for a model wall by the stability codes.

This last result confirms two important assumptions. The first is that with respect to high frequency fluctuations the resistive wall behaves as ideal, i.e. the instability-induced eddy currents do not leak through the wall. The second is that the segmentation of the wall does not prevent, at least away from the edges, the eddy currents from reproducing the helical patterns predicted for a continuous wall. These eddy current can account for the stabilizing effects observed when the wall is fully inserted.

The presence of minor deviations from the predicted patterns has been explained. These deviations do not affect, in the case of HBT-EP, the stabilizing role of the wall, since they can be observed mainly when the wall is fully retracted. However, they reflect a limitation of the numerical codes used, and might be more important for other experiments that plan to use a thick, segmented wall to stabilize the external kink, and are being designed using the same codes for the stability modeling.

6.2 Suggestions for Future Work

The stability calculations reported in this thesis indicated that when the HBT-EP wall is fully inserted the critical β_N to $n = 1$ external kink is well beyond values that can be reached in a plasma with ohmic heating only. To this end, future plans for the HBT-EP experiment include the installment of an antenna for ICRF heating, as a method to achieve higher values of β_N and test the stability boundary in configurations with the wall inserted.

At present, the residual, slowly growing external instabilities observed when the wall is fully inserted have not been understood. The growth rate being close to the resistive time scales of both the wall and the plasma complicates the identification of these modes. On the other hand, since the value of β_N lies between the critical β_N's calculated with and without the wall and since the magnetic structure of these slowly growing modes appears external, the residual instabilities seem best identified as resistive wall modes. However this

identification is contradicted by the large rotation frequency of the modes, for which the wall has been shown to behave as ideal.

Numerical codes able to include the effects of plasma flow, mode rotation, plasma and wall resistivity might provide additional information to assist the interpretation of these slowly growing modes. It should be noted, however, that at this time there is no established stability code that is able to model all the aspects of the HBT-EP wall, which is at the same time resistive, thick, and with poloidal and toroidal structure.

The resistive wall mode hypothesis could also be tested by (1) by changing the rotation frequency of the external modes with resonant magnetic perturbations applied with HBT-EP's modular saddle coil system or (2) by replacing the aluminum wall segments with material having a higher resistivity (e.g. stainless steel). The rotation control method has already been applied successfully to internal instabilities [55], and experiments are planned for HBT-EP that make use of a wall with an "adjustable" time constant. In these upcoming experiments, one half of HBT-EP's wall segments will be replaced by stainless steel segments. The thickness of the stainless steel segments (2.5 mm) was selected to be less than the skin-depth of the induced eddy currents and to produce a wall time constant shorter than the typical resistive instability growth time.

Improvements to the HBT-EP diagnostics now underway, will also greatly facilitate stability studies. The multi-point Thomson scattering system will measure the electron pressure profile and improve the procedure for numerical reconstruction of the equilibria. These internal measurements, together with the large set of magnetic data already attainable, might be sufficient to reconstruct uniquely the safety factor profile, thus releasing from the constraint of only being able to perform equilibrium reconstructions during sawtoothing periods of plasma discharges.

References

[1] INTERNATIONAL FUSION RESEARCH COUNCIL, in *Nuclear Fusion*, **30** (1990) 1641.

[2] KOIDE, Y., in *Bull. Am. Phys. Soc.* **41** (1996) 1419, to be published in *Phys. Plasmas*.

[3] SHEFFIELD, J., DORY, R.A., COHN, S.M., et al., in *Fusion Technology* **9** (1986) 199.

[4] TAYLOR, T.S., private communication.

[5] WESSON, J.A., in *Nuclear Fusion*, **18** (1978) 87.

[6] FREIDGERG, J.P., in *Ideal Magnetohydrodynamics*, Plenum Press, New York 1987.

[7] SYKES, A., TURNER, M.F., and PATEL, S., in *Controlled Fusion and Plasma Physics*, Eleventh European Conference, Aachen, W. Germany, p. 363 (1983).

[8] COPPI, B., FERREIRA, A., MARK, J.W., RAMOS, J.J., in *Nucl. Fusion* **19** (1979) 715.

[9] TROYON, F., GRUBER, R., SAURENMANN, H., SEMENZATO, S., SUCCI, S., in *Plasma Phys. Controll. Fusion* **26** (1984) 209.

[10] KESSEL, C., MANICKAM, J., REWOLDT, G., and TANG, W.M., in *Phys. Rev. Lett.* **72** (1994) 1212.

[11] NATIONAL SPHERICAL TOKAMAK EXPERIMENT, Status Report, 1995.

[12] NAJMABADI, F. and CONN, R.W., in *Plasma Physics and Controlled Nuclear Fusion Research*, Würzburg, 1992 (International Atomic Energy Agency, Vienna, 1993), Vol. 3, p. 295.

[13] TURNBULL, A.D., TAYLOR, T.S., LIN-LIU, Y.R., and ST. JOHN, H., in *Phys. Rev. Lett.* **74** (1995) 718.

[14] JET TEAM, in *Plasma Physics and Controlled Nuclear Fusion Research*, Würzburg, 1992 (International Atomic Energy Agency, Vienna, 1993), Vol. 1, p. 15.

[15] ROSENBLUTH, M.N., HOGAN, J., BOUCHER, D., et al., in *Plasma Physics and Controlled Nuclear Fusion Research*, Seville, 1994 (International Atomic Energy Agency, Vienna, 1995), Vol. 2, p. 517.

[16] NALESSO, G.F., COSTA, S., in *Nuclear Fusion*, **20** (1980) 443.

[17] GIMBLETT, C.G., in *Nuclear Fusion*, **26** (1986) 617.

[18] HENDER, T.C., GIMBLETT, C.G., ROBINSON, D.C., in *Nuclear Fusion*, **29**, (1989) 1279.

[19] BETTI, R., and FREIDBERG, J.P., in *Phys. Rev. Lett.*, **74** (1995) 2949.

[20] FINN, J.M., in *Phys. Plasmas* **2** (1995) 3782.

[21] BOOZER, A.H., in *Phys. Plasmas* **2** (1995) 4521.

[22] BONDESON, A. and WARD, D.J., in *Phys. Rev. Lett.*, **72** (1994) 2709.

[23] STRAIT, E.J., TAYLOR, T.S., TURNBULL, A.D., et al., in *Phys. Rev. Lett.*, **74** (1995) 2483.

[24] OKABAYASHI, M., POMPHREY, N., MANICKAM, J., et al., in *Nuclear Fusion*, **36** (1994) 1167.

[25] FITZPATRICK, R., in *Phys. Plasmas* **1** (1994) 2931.

[26] MAUEL, M.E., EISNER, E., GAROFALO, A., et al., presented at the Sixteenth International Conference on Plasma Physics and Controlled Nuclear Fusion Research, Montreal, 1996 (to be published).

[27] VIJAYA SANKAR, M.K., EISNER, E., GAROFALO, A., et al., in *Journal of Fusion Energy*, Vol. 12, No. 3, 1993.

[28] GATES, D., PhD thesis, Columbia University, New York, 1993.

[29] IVERS, T.H., EISNER, E., GAROFALO, A., et al., in *Phys. Plasmas*, **3** (1996) 1926.

[30] SHAFRANOV, V.D., in *Plasma Physics and the Problem of Controlled Thermonuclear Reactions* (Pergamon Press, New York), Vol. 1 (1958).

[31] MAUEL, M.E., et al., in *Plasma Physics and Controlled Nuclear Fusion Research*, Nice, 1988 (International Atomic Energy Agency, Vienna, 1989), Vol. 1, p. 415.

[32] LAO, L.L., ST. JOHN, H., STAMBAUGH, R.D., KELLMAN, A.G., PFEIFFER, W., in *Nucl. Fusion* **25** (1985) 1611.

[33] BERNSTEIN, I.B., FRIEMAN, E.A., KRUSKAL, M.D., and KULSRUD, R.M., in *Proc. R. Soc. London, Ser. A* **244** (1958) 17.

[34] GOEDBLOED, J.P., in *Lecture Notes on Ideal Magnetohydrodynamics*, Fom-Instituut voor Plasmafysica, Nieuwegein, Netherlands (1979).

[35] FURTH, H.P., KILLEN, J., ROSENBLUTH, M.N., COPPI, B., in *Plasma Physics and Controlled Nuclear Fusion Research*, 1964 (International Atomic Energy Agency, Vienna, 1965), Vol. 1, p. 103.

[36] GREEN, J.M., and JOHNSON, J.L., in *Plasma Phys.* **10** (1968) 729.

[37] FREIDBERG, J.P. and BETTI, R., Plasma Seminar at Columbia University, New York, March 1994.

[38] GRIMM, R.C., GREEN, J.M., JOHNSON, J.L., in *Methods in Computational Physics*, Vol.16 (KILLEEN, J., Ed.) Academic Press. New York (1976) 253.

[39] MANICKAM, J., GRIMM, R.C., DEWAR, R.L., in *Computer Physics Communications*, **24** (1981) 355.

[40] CHANCE, M.S., to be published in *Nucl. Fusion*.

[41] TODD, A.M.M., CHANCE, M.S., GREEN, J.M., GRIMM, R.C., JOHNSON, J.L., and MANICKAM, J., in *Phys. Rev. Lett.*, **38** (1977) 826.

[42] TODD, A.M.M., MANICKAM, J., OKABAYASHI, M., et al., in *Nucl. Fusion* **19** (1979) 743.

[43] ROBINSON, D.C., et al., in *Plasma Physics and Controlled Nuclear Fusion Research*, Kyoto, 1986 (International Atomic Energy Agency, Vienna, 1987), Vol. 1, p. 575

[44] NAVRATIL, G.A., et al., in *Plasma Physics and Controlled Nuclear Fusion Research*, Kyoto, 1986 (International Atomic Energy Agency, Vienna, 1987), Vol. 1, p. 299.

[45] GAROFALO, A., EISNER, E., GATES, D., et al., in *Bull. Am. Phys. Soc.* **38**, (1993) 2006.

[46] IVERS, T.H., PhD thesis, Columbia University, New York, 1991.

[47] KOMBARGI, R., PhD thesis, Columbia University, New York, 1997.

[48] OKABAYASHI, M. POMPHREY, N., MANICKAM, J., et al., in *Nucl. Fusion* **36** (1996) 1167.

[49] EISNER, E., BAI, L., GAROFALO, A., et al., in *Bull. Am. Phys. Soc.* **38**, (1993) 2007.

[50] LAZARUS, E.A., LISTER, J.B., NEILSON, G.H., in *Ecole Polytechnique Federale De Lausanne report* LRP 376/89, Switzerland, May 1989.

[51] NAGAYAMA, Y., NAITO, M., UEDA, Y., et al., in *Nucl. Fusion* **24** (1984) 1243.

[52] MIGLIUOLO, S., in *Nucl. Fusion* **33** (1993) 1721.

[53] O'ROURKE, J., in *Plasma Phys. Control. Fusion* **33** (1991) 289.

[54] IVERS, T.H., GATES, D., MARSHALL, T.C., et al., in *Plasma Physics and Controlled Nuclear Fusion Research*, Washington, DC, 1990 (IAEA, Vienna, 1991), Vol. 1, p. 573.

[55] IVERS, T.H., EISNER, E., GAROFALO, A., et al., in *Bull. Am. Phys. Soc.* **41** (1996) 1511.